



Interpreting the Si II and C II Line Spectra from the COS Legacy Archive Spectroscopic Survey Using a Virtual Galaxy from a High-resolution Radiation-hydrodynamic Simulation

Simon Gazagnes¹ , Valentin Mauerhofer² , Danielle A. Berg¹ , Jeremy Blaizot³ , Anne Verhamme⁴ , Thibault Garel⁴ , Dawn K. Erb⁵ , Karla Z. Arellano-Córdova¹ , Jarle Brinchmann⁶ , John Chisholm¹ , Matthew Hayes⁷ , Alaina Henry⁸ , Bethan L. James⁹ , Anne Jaskot¹⁰ , Nika Jurlin¹ , Crystal L. Martin¹¹ , Michael Maseda¹² , Claudia Scarlata¹³ , Evan D. Skillman¹³ , Stephen M. Wilkins¹⁴ , Aida Wofford¹⁵ , and Xinfeng Xu¹⁶

¹ Department of Astronomy, The University of Texas at Austin, 2515 Speedway, Stop C1400, Austin, TX 78712-1205, USA; gazagnes@utexas.edu

² Kapteyn Astronomical Institute, University of Groningen, P.O Box 800, 9700 AV Groningen, The Netherlands

³ Centre de Recherche Astrophysique de Lyon UMR5574, F-69230, Saint-Genis-Laval, France

⁴ Department of Astronomy, University of Geneva, 51 Chemin Pegasi, 1290 Versoix, Switzerland

⁵ The Leonard E. Parker Center for Gravitation, Cosmology, and Astrophysics, Department of Physics, University of Wisconsin-Milwaukee, 3135 N Maryland Avenue, Milwaukee, WI 53211, USA

⁶ Instituto de Astrofísica e Ciências do Espaço, Universidade do Porto, CAUP, Rua das Estrelas, PT4150-762 Porto, Portugal

⁷ Stockholm University, Department of Astronomy and Oskar Klein Centre for Cosmoparticle Physics, AlbaNova University Centre, SE-10691, Stockholm, Sweden

⁸ Space Telescope Science Institute, 3700 San Martin Drive, Baltimore, MD 21218, USA

⁹ AURA for ESA, Space Telescope Science Institute, 3700 San Martin Drive, Baltimore, MD 21218, USA

¹⁰ Department of Astronomy, Williams College, Williamstown, MA 01267 USA

¹¹ Department of Physics, University of California Santa Barbara, Santa Barbara, CA 93106, USA

¹² Department of Astronomy, University of Wisconsin-Madison, 475 N. Charter Street, Madison, WI 53706, USA

¹³ Minnesota Institute for Astrophysics, University of Minnesota, 116 Church Street SE, Minneapolis, MN 55455, USA

¹⁴ Astronomy Centre, University of Sussex, Falmer, Brighton BN1 9QH, UK

¹⁵ Instituto de Astronomía, Universidad Nacional Autónoma de México, Unidad Académica en Ensenada, Km 103 Carr. Tijuana-Ensenada, Ensenada 22860, México

¹⁶ Center for Astrophysical Sciences, Department of Physics & Astronomy, Johns Hopkins University, Baltimore, MD 21218, USA

Received 2023 March 10; revised 2023 May 22; accepted 2023 May 29; published 2023 July 27

Abstract

Observations of low-ionization state metal lines provide crucial insights into the interstellar medium (ISM) of galaxies, yet, disentangling the physical processes responsible for the emerging line profiles is difficult. This work investigates how mock spectra generated using a single galaxy in a radiation-hydrodynamical simulation can help us interpret observations of a real galaxy. We create 22,500 C II and Si II spectra from the virtual galaxy at different times and through multiple lines of sight and compare them with the 45 observations of low-redshift star-forming galaxies from the COS Legacy Spectroscopic Survey (CLASSY). We find that the mock profiles provide accurate replicates of the observations of 38 galaxies with a broad range of stellar masses (10^6 – $10^9 M_\odot$) and metallicities (0.02–0.55 Z_\odot). Additionally, we highlight that aperture losses explain the weakness of the fluorescent emission in several CLASSY spectra and must be accounted for when comparing simulations to observations. Overall, we show that the evolution of a single simulated galaxy can produce a large diversity of spectra whose properties are representative of galaxies of comparable or smaller masses. Building upon these results, we explore the origin of the continuum, residual flux, and fluorescent emission in the simulation. We find that these different spectral features all emerge from distinct regions in the galaxy’s ISM, and their characteristics can vary as a function of the viewing angle. While these outcomes challenge simplified interpretations of down-the-barrel spectra, our results indicate that high-resolution simulations provide an optimal framework to interpret these observations.

Unified Astronomy Thesaurus concepts: [Ultraviolet astronomy \(1736\)](#); [Interstellar medium \(847\)](#); [Starburst galaxies \(1570\)](#)

1. Introduction

The interstellar medium (ISM) of star-forming galaxies is an intricate environment, constantly transformed by complex processes such as star formation and evolution, galactic outflows, and gas accretion. Understanding what regulates the ISM transformation through time is crucial for establishing accurate galaxy evolution models. Yet this effort relies on our ability to extract robust and accurate insights into their properties. In this context, low-ionization states (LIS) of metals

such as C II (ionization potential between 11.26 and 24.38 eV), Si II (ionization potential between 8.15 and 16.34 eV), or Fe II (ionization potential between 7.90 and 16.19 eV) are powerful tracers of the neutral and low-ionization ISM: their associated transitions, most of which span the ultraviolet (UV) and far-UV wavelength regions, provide us with direct insights into the gas properties such as its metallicity, its geometry, or its kinematics.

The typical approach to extracting insights from LIS metal lines is to analyze the *down-the-barrel* absorption lines. The properties and shape of the absorption features are tightly connected to the gas velocity, column density, and covering fraction, which all describe different aspects of the galaxy’s ISM. For example, the observation of broad blueshifted absorption lines suggests the presence of outflowing gas (e.g., Heckman et al. 2000, 2015; Shapley et al. 2003;



Original content from this work may be used under the terms of the [Creative Commons Attribution 4.0 licence](#). Any further distribution of this work must maintain attribution to the author(s) and the title of the work, journal citation and DOI.

Rubin et al. 2011; Erb et al. 2012; Wofford et al. 2013; Chisholm et al. 2015, 2016, 2017b; Finley et al. 2017a; Steidel et al. 2018; Wang et al. 2020; Xu et al. 2022). The analysis of the outflow properties (e.g., speed, structure, and ejected mass) can help us understand the baryon cycle of galaxies, (i.e., the interplay between the outflow rates, gas accretion rate, and their impact on the star formation rate (SFR), see, e.g., Oppenheimer et al. 2010). By combining column densities of LIS lines with neutral hydrogen, one can measure the metal content of the neutral gas, where a large proportion of the baryonic component is thought to lie. Also, by comparing these line properties with the ionized gas abundances, one can decipher mixing timescales between the two phases and ultimately, the metal enrichment of the ISM (e.g., James et al. 2014; Chisholm et al. 2018; James & Aloisi 2018).

LIS absorption lines are relevant in the context of reionization studies. The observation of absorption features with large residual flux (i.e., the amount of flux at the maximum depth of the line) may probe the presence of low-column density channels through which ionizing photons can escape the ISM of the galaxy (e.g., Heckman et al. 2001; Alexandroff et al. 2015; Reddy et al. 2016; Chisholm et al. 2018; Gazagnes et al. 2018; Steidel et al. 2018; Mauerhofer et al. 2021; Saldana-Lopez et al. 2022). This aspect makes LIS absorption lines promising diagnostics for predicting the escape fraction of ionizing photons ($f_{\text{esc}}^{\text{LyC}}$) at high redshift where it cannot be directly measured due to the opacity of the intergalactic medium.

Though UV LIS resonant lines are a common approach to exploring the ISM properties of star-forming galaxies, one can also explore the UV LIS *fluorescent* line properties. Many LIS metal ions are not entirely resonant: their ground state is split into two spin levels (the level just above the ground state is referred to as the fine-structure level), providing an additional channel of photon (de-)excitation. Since the energy level difference of this fluorescent channel is smaller than for the resonant channel, we observe an additional spectral feature redder than the LIS absorption line,¹⁷ which provides distinct but complementary insights into the physical conditions within the galaxies.

In recent years, multiple works have reported the detection of fluorescent emission in star-forming galaxies from $z \sim 0$ –5.5 (Shapley et al. 2003; Erb et al. 2010, 2012; Rubin et al. 2011; Martin et al. 2012; James et al. 2014; Jaskot & Oey 2014; Bosman et al. 2019; Jaskot et al. 2019; Wang et al. 2020). Simultaneously, several studies used idealized outflow/inflow models or radiation-hydrodynamic simulations to investigate the factors regulating the observed strength of the fluorescent emission (Prochaska et al. 2011; Scarlata & Panagia 2015; Mauerhofer et al. 2021; Carr & Scarlata 2022). Both simulations and observations highlighted that the fluorescent spectral features can trace the presence of outflowing gas, inform about the gas column density along the line of sight, and importantly, provide clues into the spatial distribution of the absorbing gas (see, e.g., the discussion in Jaskot & Oey 2014; Rivera-Thorsen et al. 2015).

Although UV LIS absorption and emission lines have a high and valuable informative potential for constraining the properties of a galaxy’s ISM, LIS metal line spectra remain difficult to interpret. The emerging profiles can exhibit complex, asymmetric shapes that result from the contributions of multiple gas clouds. Such clumpy configuration challenges simple interpretations of the line profiles. For example, it impacts the

residual flux measurements so that one can only infer from them an upper limit to the geometric covering fraction (see, e.g., Vasei et al. 2016; Rivera-Thorsen et al. 2017; Gazagnes et al. 2018). Additionally, commonly studied LIS lines (e.g., Si II 1260 Å, C II 1334 Å) are resonance lines that may be affected by *emission filling* (scattered line photons reemitted in the line-of-sight direction, see, e.g., Prochaska et al. 2011; Erb et al. 2012; Scarlata & Panagia 2015), which affects both the shape and properties of the absorption line. Finally, the analysis of the fluorescent emission also suffers some caveats. In particular, the fluorescent emission is typically more spatially extended than the continuum emission (Erb et al. 2012; Finley et al. 2017a; Wang et al. 2020), which makes its strength particularly sensitive to aperture losses (Prochaska et al. 2011; Erb et al. 2012; Finley et al. 2017b; Wang et al. 2020; Mauerhofer et al. 2021). Therefore, while the absorption and emission line analysis often relies on simple spectral diagnostics (e.g., the equivalent width or the residual flux) or idealized models, these approaches might only capture a fraction of the full information content available.

The maturity of recent simulation techniques has enabled a significant step forward in disentangling the physical processes responsible for the absorption and emission line shapes. In particular, Mauerhofer et al. (2021, hereafter, M21) provided a thorough analysis of the physics that govern the production of neutral and LIS line spectra using a high-resolution radiation hydrodynamics (RHD) simulation post-processed with radiative-transfer techniques. Their work provided crucial lessons for interpreting rest-frame UV and FUV spectra, uncovering major findings for the era of high-redshift observations with JWST or with future 40 m class telescopes. Importantly, such a framework now enables us to thoroughly compare simulated spectra constructed from realistic galaxy environments to actual observations. For example, Blaizot et al. (2023) recently highlighted the remarkable consistency between the Ly α profiles seen in the simulation of M21 and the Ly α observations of low- z star-forming galaxies.

In the present paper, we investigate whether the M21 simulation is able to reproduce the C II and Si II spectra of 45 low-redshift star formation galaxies from the COS Legacy Spectroscopic Survey (CLASSY; Berg et al. 2022) whose properties are similar to high- z objects. Showing that it can, we further use the simulation to develop an interpretation of these complex observations. In particular, we explore the effects of limited aperture size, the time and sightline variations of the spectral properties, and the origin of the different spectral features that compose an LIS line spectrum.

This paper is organized as follows: Section 2 details the simulation setup and the observations used in this work. Section 3 compares the Si II and C II properties and line profiles in the simulated and observed spectra, and Section 4 analyzes the impact of aperture loss on the fluorescence emission properties. Section 5 discusses the variety of LIS line profiles generated using a single virtual galaxy and explores the spatial properties of the stellar continuum, fluorescent emission, and residual flux in the simulation. Finally, Section 6 summarizes our results.

2. Data

The goal of this work is to compare the C II $\lambda 1334$ +C II* $\lambda 1335$ and Si II $\lambda 1260$ +Si II* $\lambda 1265$ line profiles from the CLASSY observations to physically realistic models. To do so, we construct 22,500 mock UV spectra using the simulated

¹⁷ Fluorescent transitions are commonly indicated with a star, e.g., Si II*, C II*, or Fe II*.

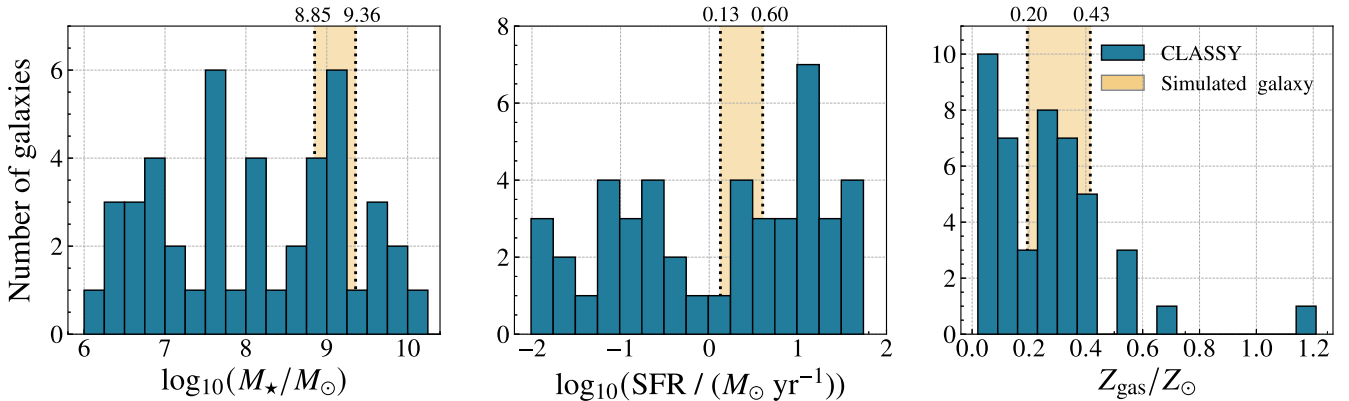


Figure 1. The range of stellar masses (M_*), SFRs, and ionized gas metallicity (Z_{gas}) of the CLASSY sample (blue histogram) and of the virtual galaxy (orange stripe) in the zoom-in simulation during the 750 Myr ($z = 4.19$ to $z = 3.00$) period considered in this work.

galaxy in the high-resolution RHD simulation from M21 and explore their resemblance with the CLASSY spectra. Section 2.1 describes the CLASSY sample and Section 2.2 details the simulation.

2.1. Observations

CLASSY (Berg et al. 2022) is a Hubble Space Telescope/Cosmic Origins Spectrograph (HST/COS) treasury program that provided the first high-resolution, high signal-to-noise far-UV (FUV) spectral catalog of 45 local star-forming galaxies spanning similar properties as reionization-era objects in terms of masses ($\log(M_*/M_\odot) \approx 6\text{--}10$), gas metallicities ($0.02\text{--}1.2 Z_\odot$), SFRs ($\log(\text{SFR}) \approx -2.0$ to $+1.5$), and ionization parameters ($\log(U) \approx -3.3$ to -2.0). Figure 1 provides more details into the distributions of stellar masses, SFR, and gas metallicities for the 45 CLASSY objects. The CLASSY spectra cover a rest-frame wavelength range from ~ 1200 to 2000\AA , utilizing the full potential of the G130M+G160M+G185M gratings on HST/COS. The high data quality makes these observations ideal laboratories for determining the most promising FUV diagnostics for interpreting high-redshift observations.

All the CLASSY data, including 135 new and 177 archival orbits, were reduced consistently using CALCOS v3.3.101. A complete description of the data reduction procedure is detailed in Berg et al. (2022), and a thorough technical overview of the different challenges is given in James et al. (2022). All observational data presented in this paper were obtained from the Mikulski Archive for Space Telescopes (MAST) at the Space Telescope Science Institute. The observations can be accessed via [10.17909/m3fq-jj25](https://doi.org/10.17909/m3fq-jj25).

Because of detector gaps or Milky Way absorption line contamination, the wavelength region around 1260 or 1334 \AA is not always usable for our analysis. Of the 45 galaxies, 39 and 37 have *non-contaminated* C II $\lambda 1334$ and Si II $\lambda 1260$ observations, respectively, and 32 have both wavelength regions observed simultaneously. All 45 galaxies have at least one of the two wavelength ranges covered, and we, therefore, consider the whole sample in our analysis. The next section details the RHD simulation setup.

2.2. Simulation

In M21, the authors use one galaxy from a zoom-in simulation to investigate the processes responsible for the

shape of the Lyman- β and C II $\lambda 1334 + \text{C II}^* \lambda 1335$ lines and discuss their results in the context of the escape of ionizing photons. In this work, we use the same framework to build a large data set of 22,500 mock spectra that we compare to the CLASSY observations. Section 2.2.1 presents the zoom-in simulation and Section 2.2.2 details the steps used to generate the mock spectra, building upon the strategy from M21 and Blaizot et al. (2023).

2.2.1. Zoom-in Simulation

The M21 simulation run was obtained with the adaptive mesh refinement code RAMSES-RT (Teyssier 2002; Rosdahl et al. 2013; Rosdahl & Teyssier 2015). The initial conditions were generated using MUSIC (Hahn & Abel 2013) and chosen such that the resulting galaxy has a stellar mass of $M_* \sim 10^9 M_\odot$ at $z = 3$, with a maximum cell resolution of 14 pc around this redshift. The simulation builds upon the physics of cooling, supernova feedback, and star formation from SPHINX (Rosdahl et al. 2018), and includes a self-consistent propagation of the ionizing photons through radiative transfer providing accurate nonequilibrium ionization states of hydrogen and helium atoms as well as radiative feedback. The ionizing radiation emission from stellar particles follows the BPASS 2.0 stellar library models (Eldridge et al. 2008; Stanway et al. 2016), which have a maximum (cutoff) M_* of $100 M_\odot$, with all stars set in binary systems. An additional ionizing UV background is added to all cells that have a density of hydrogen $n_{\text{H}} < 10^{-2} \text{ cm}^{-3}$ to account for the ionizing radiation produced by external galaxies in a realistic universe (Faucher-Giguère et al. 2009).

We use 75 simulation outputs from $z = 4.19\text{--}3.00$ (~ 9.2 Myr time steps). Over this period, the halo mass evolves from 4.0×10^{10} to $5.6 \times 10^{10} M_\odot$, the stellar mass increases from 7.1×10^8 to $2.3 \times 10^9 M_\odot$, and both the averaged stellar and gas metallicity increase from 0.20 to $0.42 Z_\odot$. Additionally, during these 690 Myr, the SFR (SFR, measured using all stars whose age is less than 100 Myr) oscillates between ~ 1.5 and $4.0 M_\odot \text{ yr}^{-1}$, with two main SFR peaks around 1.64 and 2.04 Gyr.

Figure 1 compares the range of stellar mass, SFR, and gas metallicities in the virtual galaxy and in the CLASSY sample. While the virtual galaxy covers a narrower range of galaxy properties compared to the CLASSY sample, the 75 outputs considered in this work enable us to generate mock spectra at different phases in the galaxy evolution, which is interesting in

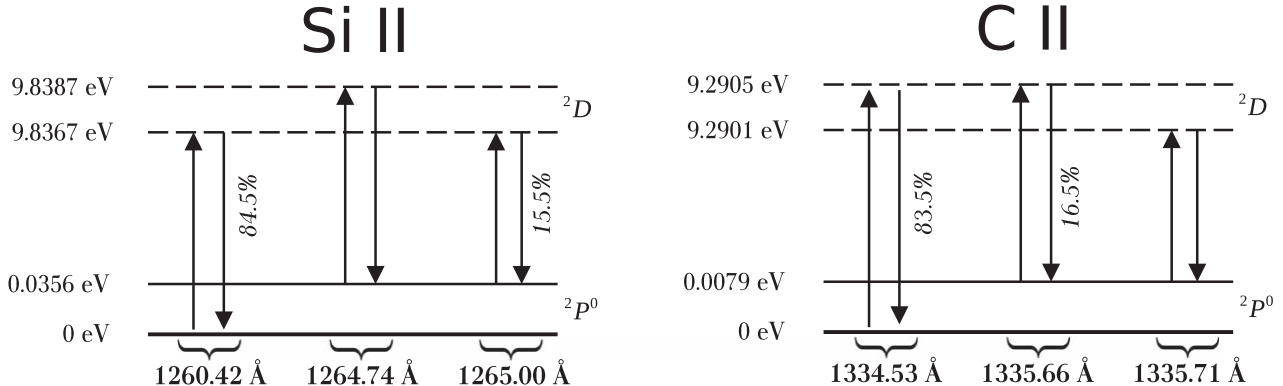


Figure 2. Energy levels of the Si II and C II ions, illustrating the different channels of excitation and de-excitation from the ground-state or fine-structure level. The percentage values indicate the probabilities that an electron from the excited level is de-excited to the ground-state (resonance) or to the fine-structure level (fluorescence). A photon absorbed at 1260.42 Å (1334.53 Å) has a 15.5% (16.5%) chance to be reemitted at the wavelength of the fluorescence for Si II (C II). Figure adapted from M21.

the context of understanding the physical processes required to produce realistic LIS metal lines observations. Additionally, CLASSY galaxies are at z between 0.002 and 0.182; hence, a significantly lower redshift range than the range considered for the simulated galaxy ($z = 4.19\text{--}3.00$). However, the CLASSY targets have been selected to span similar properties as seen at high redshift, with, in particular, SFRs that are more typical of galaxies at cosmic noon (see Figure 2 in Berg et al. 2022). In addition, absorbing gas near the brightest stars dominates the down-the-barrel spectrum, so cosmological contexts that normally affect the circumgalactic medium (CGM) gas may not be as significant for our analysis. Finally, in the 690 Myr period considered in this work, we note that the virtual galaxy did not experience any major merging events which could have significantly transformed its environment and made more difficult the interpretation of the line profiles. Similarly, in CLASSY, most of the targets are simple, isolated structures, suggesting that these objects did not undergo any recent major merging events. We detail in the next section the procedure to create the mock C II and Si II profiles.

2.2.2. Creating the Mock Observations

In order to produce mock spectra, we first need to compute the number densities of C^+ and Si^+ ions everywhere in the simulation. We do this in two steps: first, we derive the number density of each element (n_{C} and n_{Si}), and then we compute their ionization fractions. We derive the densities of carbon and silicon in each simulation cell assuming solar abundance ratios, such that $n_{\text{C}} = n_{\text{H}} A_{\text{C}} Z_{\text{cell}} / Z_{\odot}$ and $n_{\text{Si}} = n_{\text{H}} A_{\text{Si}} Z_{\text{cell}} / Z_{\odot}$, where A_{C} and A_{Si} are, respectively, the solar ratio of carbon (2.69×10^{-4}) and silicon atoms (3.24×10^{-5}) over hydrogen atoms taken from Asplund et al. (2021), Z_{\odot} is the solar metallicity (0.0134, Grevesse et al. 2010), and Z_{cell} is the value of the metal mass fraction in each cell. While not included in M21, this work also considers the phenomenon of dust depletion: large fractions of metals are incorporated into dust grains and hence removed from the ISM gas. We adopt the depletion fraction of metals as a function of gas-phase metallicity from De Cia et al. (2016) and Konstantopoulou et al. (2022; $X_{\text{Si}}^{\text{dust}} = 1 - 10^{-0.04 - 0.72 * (1.09 + 0.60Z)}$ and $X_{\text{C}}^{\text{dust}} = 1 - 10^{-0.1 * (1.09 + 0.60Z)}$) and apply the correction formula cell by cell in the simulation. We note that both observations (Jenkins 2009; Parvathi et al. 2012) and simulations (Choban et al. 2022) highlighted that dust-

depletion fractions also depend on the average gas density along the line of sight. In this work, we do not apply a density-dependent model for the depletion fractions as there currently does not exist simple implementations of such models. Yet, as further discussed below, we tested and compared different sets of mock spectra generated using different models. In the context of dust depletion, while we do observe some slight differences in the distribution of spectral properties that are generated, we do not find that it affects the results related to the comparison of the CLASSY sample, which is the main focus of this work.

The ionization fractions of carbon and silicon are computed using KROME (Grassi et al. 2014) using the recombination rates from Badnell (2006), the collisional ionization rates from Voronov (1997), and the photoionization cross-sections from Verner et al. (1996). The complete details of this procedure are given in M21. Note that KROME assumes chemical equilibrium for both ions. To account for potential effects from nonequilibrium ionization states for Si II and C II, one would have to self-consistently propagate these elements in the RAMSES-RT simulation run, which is not trivial. Yet, accounting for nonequilibrium ionization states would mostly affect the diffuse gas which, in theory, has little impact on the absorption spectra (emerging from denser gas).

As noted in the introduction, the ground-state energy level of the C II and Si II ions is split into two spin states having an energy difference of 0.0079 eV for C II and 0.0356 eV for Si II (see Figure 2). These fine-structure levels, typically populated through electron collisions, produce two additional channels (referred to as fluorescent channels, noted as C II* and Si II*) of photon absorption and emission at 1335.66 and 1335.71 Å, respectively, for C II, and at 1264.73 and 1265.02 Å, respectively, for Si II. Typically, the phenomenon of fluorescence works as follows: a photon absorbed at 1260.42 or 1334.53 Å can either be reemitted at the same wavelength (resonance) or at the wavelength of the fine-structure level (fluorescence). The probability of either phenomenon depends on the transitions' Einstein coefficients, and the probability of resonance scattering is higher than for the fluorescence (84.5% and 83.5% for Si II and C II, respectively). Typically, fluorescent emission emerges from regions where resonant photons undergo multiple scatterings and are converted to fluorescent emission (Scarlata & Panagia 2015).

Fluorescent lines are usually observed as emission lines (e.g., Shapley et al. 2003; Erb et al. 2010; Jones et al. 2012; Martin et al. 2012; Finley et al. 2017b; Wang et al. 2020), yet, the physics of the fine-structure levels depends on a variety of factors (e.g., density, dust, radiation fields) such that in some cases, absorption features dominate (Wolfe et al. 2003; Lebouteiller et al. 2013; Gatkine et al. 2019; Jaskot et al. 2019; Xu et al. 2023). This is because, as emphasized in Figure 2, the first energy level is also split in two such that there exist two additional channels of excitation for an electron in the fine-structure level. Similar to M21, we consider the physics of all resonant and nonresonant channels of C II and Si II when applying the radiative transfer post-processing. The percentage of ions being in the fine-structure level is determined using PYNEB (Luridiana et al. 2015) assuming the default atomic data.

To produce the LIS absorption and emission lines in any direction, we use the radiative transfer post-processing code RASCAS (Michel-Dansac et al. 2020). RASCAS produces the line profiles using the following procedure: 1 million photon packets sample the spectra of stellar populations contained in each star particle, within a wavelength range of $\pm 10 \text{ \AA}$ around the C II $\lambda 1334$ and Si II $\lambda 1260$ lines. The photon packets are assigned to stars with a probability that scales with the star particle luminosity. Their position is assigned to the position of the stellar particles in the simulation and their initial direction is drawn from an isotropic distribution. The frequency of the photon packet is drawn randomly from a power law based on the stellar energy distribution of the BPASS model with age and metallicity equal to those of the particle. Photon packets are propagated through the simulation grid and encounter at each cell an optical depth, which is the sum of all channels of interaction:

$$\tau_{\text{cell}} = \tau_{\text{C II} 1334.53} + \tau_{\text{C II}* 1335.66} + \tau_{\text{C II}* 1335.71} + \tau_{\text{Si II} 1260.42} + \tau_{\text{Si II}* 1264.73} + \tau_{\text{Si II}* 1265.02} + \tau_{\text{dust}}. \quad (1)$$

The optical depth of each line is the product of the ion column density in each cell and the ion cross section, which is defined by Equation (2) in M21.¹⁸

We compute the turbulent velocity of the gas (v_{turb}) and the optical depth of the dust grains (τ_{dust}) in each cell. We determine v_{turb} using a formula that accounts for the gas density and velocity in the neighboring cells, as in the star formation recipe of, e.g., Trebitsch et al. (2021). This method provides a more physical prescription of v_{turb} than M21 whose authors assumed a fixed value of 20 km s^{-1} . This model results in a broader range of v_{turb} , which varies from a few kilometers per second to hundreds of kilometers per second. For τ_{dust} , we follow the implementation of Katz et al. (2022), inspired by the results of Rémy-Ruyer et al. (2014), which adopts a broken power-law function of the metallicity and is set to 0 in cells with temperatures above 10^5 K . This temperature cut is not applied when calculating the dust-depletion fractions. Nevertheless, because the number densities of C+ and Si+ in cells with $T > 10^5 \text{ K}$ are relatively small (3% of C and $\sim 0.1\%$ of Si, see Mauerhofer 2021) in this simulation, we assume that applying this cut would not impact our results.

M21 shows that the choice of turbulence and dust models can significantly impact the shape and properties of the absorption and emission lines produced. We, therefore, tested

how our results are affected by using different radiative-transfer *recipes* to produce the line profiles (e.g., varying the dust model or v_{turb} parameter, accounting for dust depletion). We observed slight changes in the distribution of the spectral line shapes and properties depending on the model used. As a result of these preliminary tests, we found that including the dust-depletion fractions and calculating v_{turb} and τ_{dust} using the approaches described in the current work seem to provide a more accurate description of the environments of the CLASSY galaxies (i.e., the best similarity between the simulated and observed line shapes and properties). Yet, importantly, we also noticed that using any of these models would still provide similar outcomes so that the main conclusions drawn in this work would not be affected. Because determining the impact of different recipes on the properties of the simulated spectra is an important aspect of providing physically realistic models of the environments of star-forming galaxies, an upcoming paper (V. Mauerhofer et al. 2023, in preparation) will detail the results of the additional tests performed in the context of this work.

We compute the radiative transfer of the UV continuum through the simulated galaxy and its ISM/CGM in post-processing. In practice, we emit photon packets from all the star particles located within the virial radius ($R_{\text{vir}} = 28 \text{ kpc}$) and compute their propagation and scattering until they reach $3 \times R_{\text{vir}}$ or are absorbed by dust. Along the process, we use the peeling-off technique to construct spectra in 300 directions (corresponding to a regular sampling of the sphere obtained with HealPix) and within an aperture of $1''$ diameter ($\sim 7 \text{ kpc}$ at $z = 4.2$ and 7.9 kpc at $z = 3$), which is large enough to capture the full ISM extent of the simulated galaxy, plus some of the light scattered in the CGM.¹⁹ In total, we construct 22,500 C II and Si II mock spectra based on 300 different lines of sight observations of each of the 75 simulation outputs. In all this work, we use the noiseless, synthetic spectra, but adapt their resolution to that of the CLASSY spectra (see details in Section 3). In the next section, we detail the comparison between these simulated mock profiles and the CLASSY observations.

3. Comparing the C II and Si II Line Profiles

In this section, we compare the 22,500 mock LIS spectra constructed using the simulated galaxy with the CLASSY observations. Importantly, we simultaneously compare the Si II and C II properties and profiles. This exercise is more difficult than simply looking at how well each ion property/profile is reproduced individually but provides additional insights into the accuracy of the physical models used in the simulation. Section 3.1 first compares the lines' properties and Section 3.2 determines the best-matching mock spectrum for each CLASSY observation.

3.1. Comparison of Line Properties

Here we measure and compare (i) the equivalent widths (EWs) of the C II $\lambda 1334$ and Si II $\lambda 1260$ absorption lines, (ii) the EWs of the C II* $\lambda 1335$ and Si II* $\lambda 1265$ fluorescent emission, (iii) the residual fluxes (R_f) of the absorption lines, and (iv) the absorption lines' central velocities (v_{cen}). In this work, the v_{cen} values for each line are relative to the systemic velocity of the objects, which is defined as the velocity of the

¹⁸ The C II and Si II line parameters are taken from the NIST atomic database <https://www.nist.gov/pml/atomic-spectra-database>.

¹⁹ Because the separation between ISM and CGM is not well defined, we tend to refer only to the ISM when discussing our results.

center of mass for the virtual galaxy, and as the offset velocity of the strong emission lines (e.g., H α , H β , O III) for the CLASSY galaxies.

We used a simple and consistent procedure to derive these properties for the 45 CLASSY observations and for the 22,500 mock profiles. First, the Si II and C II spectra are normalized using the median of the flux in 1 Å wide feature-free intervals around 1256 and 1331 Å, respectively. Then, we use a Gaussian line spread function to smooth all simulated spectra to a resolution of 60 km s $^{-1}$, matching the median resolution for the CLASSY spectra (see Table 3 in Berg et al. 2022). Finally, we measure each property as follows:

1. EW(C II) and EW(Si II) are derived by integrating the flux below the normalized continuum in an interval of $\pm 2.5 \text{ \AA}$ ($\approx 600 \text{ km s}^{-1}$) around $\lambda = 1334.53 \text{ \AA}$ and $\lambda = 1260.42 \text{ \AA}$, respectively.²⁰
2. EW(C II*) and EW(Si II*) are derived by integrating the flux above the normalized continuum in an interval of $\pm 2 \text{ \AA}$ ($\approx 400 \text{ km s}^{-1}$) around $\lambda = 1335.71 \text{ \AA}$ and $\lambda = 1265.02 \text{ \AA}$, respectively.
3. $R_f(\text{C II})$ and $R_f(\text{Si II})$ are obtained by taking the flux value at minimum depth of the absorption line in an interval of $\pm 2.5 \text{ \AA}$ ($\approx 600 \text{ km s}^{-1}$) around $\lambda = 1334.53 \text{ \AA}$ and $\lambda = 1260.42 \text{ \AA}$, respectively.
4. The central velocities, $v_{\text{cen}}(\text{C II})$ and $v_{\text{cen}}(\text{Si II})$, are derived by taking the velocity at which the C II $\lambda 1334$ and Si II $\lambda 1260$ absorption lines can be separated in two components holding each half the total EW. These values are relative to the systemic velocity.

Figure 3 presents an example of Si II and C II simulated spectrum with the characteristic measurements annotated. It is important to keep in mind that the EW measurements only provide information on the strength of the resonant absorption and of the fluorescent emission in the different spectra. By construction, our measurement approach always yields EW(C II) and EW(Si II) values ≥ 0 , and EW(C II*) and EW(Si II*) ≤ 0 . Consequently, spectra exhibiting pure emission around C II $\lambda 1334$ and Si II $\lambda 1260$ (due to resonant scattering) will have EW(C II) and EW(Si II) equal to 0. Similarly, spectra showing pure absorption around the C II* $\lambda 1335$ and Si II* $\lambda 1265$ will have EW(C II*) and EW(Si II*) equal to 0.

The different velocity intervals used to measure each property have been chosen to capture the maximal extent of the absorption and emission line profiles observed in the CLASSY and simulated spectra. Nevertheless, our approach has two main caveats. First, we use intervals of 600 and 400 km s $^{-1}$ to measure EW(C II) and EW(C II*), yet, the C II $\lambda 1334$ and C II* $\lambda 1335$ transitions are separated by only $\sim 250 \text{ km s}^{-1}$. Hence, absorption at the fluorescent wavelength will contribute to the value of EW(C II), and resonantly scattered emission around 1334.54 Å will contribute to the value of EW(C II*). The blending of both resonant and fluorescent contributions does not impact the Si II measurements since the Si II $\lambda 1260$ and Si II* $\lambda 1265$ transitions are separated by $\sim 1100 \text{ km s}^{-1}$.

Second, there exists a S II absorption line at 1259.52 Å, resolved in some CLASSY spectra, which is often blended with the Si II $\lambda 1260$ line. While it is typically much weaker than the Si II absorption feature, its contribution sometimes impacts the EW(Si II) and $v_{\text{cen}}(\text{Si II})$ measurements from the CLASSY

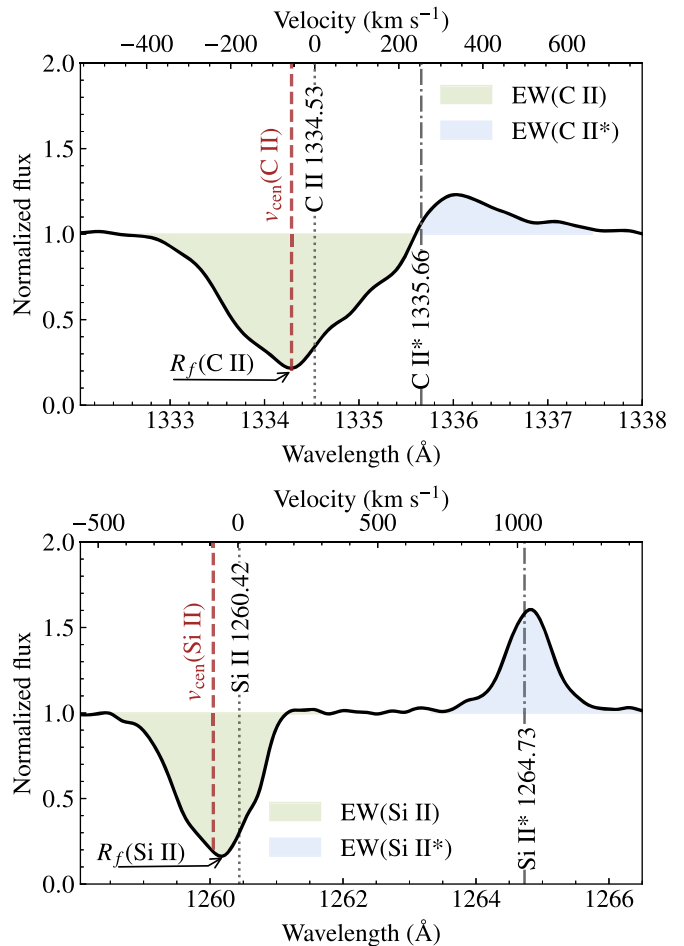


Figure 3. An example of C II (top panel) and Si II (bottom) simulated spectrum with the characteristic measurements annotated. Each spectrum has been normalized using the median of the flux in intervals around 1256 and 1331 Å for Si II and C II, respectively.

spectra. This line is not included in our radiative-transfer model.

The impact of these caveats is further discussed in the context of the joint Si II and C II properties analysis below. Overall, they do not affect the main results presented in this paper, which go beyond the simple comparison of the line spectral properties. An upcoming paper will detail the refined measurements of the LIS properties in the CLASSY spectra (K. Parker et al. 2023, in preparation).

3.1.1. Line Properties Ranges

Here we discuss the histograms of the C II and Si II properties, shown in the top and right parts of each panel of Figure 4, for CLASSY and the simulation. The range of EWs in both absorption lines (upper left panel) is typically between 0 and 2.5 Å in the simulated spectra and overlaps with most of the CLASSY measurements. We denote five CLASSY objects, with stellar masses larger than the virtual galaxy ($M_\star > 10^{9.5} M_\odot$), which have EWs $> 2.5 \text{ \AA}$. The range of residual fluxes (lower left panel) in both lines covers a similar interval for the observed and mock spectra, from 0–1. The mock line profiles have v_{cen} values between ~ -300 and 150 km s^{-1} (lower right panel). Most CLASSY galaxies have v_{cen} values

²⁰ In this work, EWs are calculated such that absorption features have positive values and emission features have negative values.

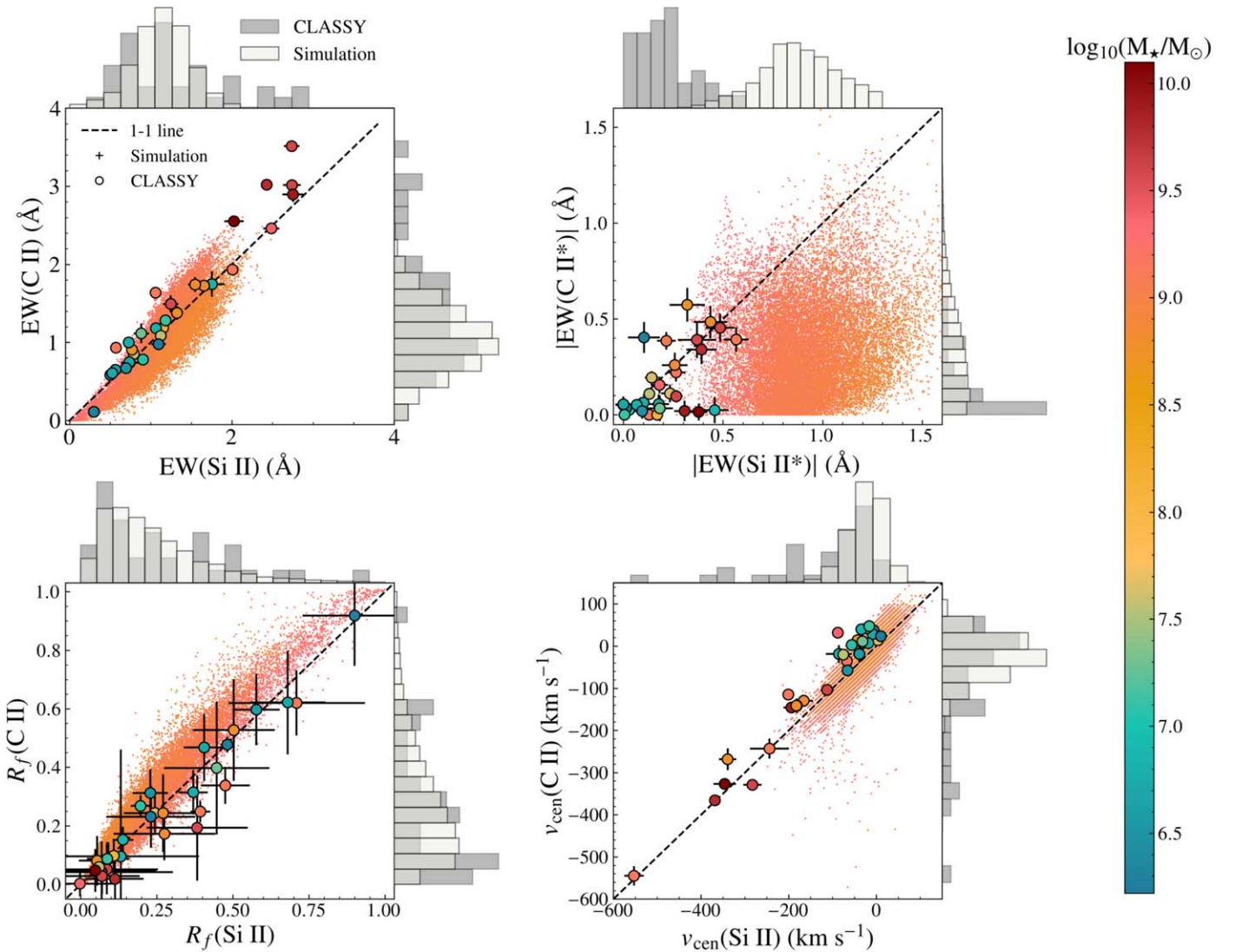


Figure 4. The comparison of the $\text{EW}(\text{C II})$ and $\text{EW}(\text{Si II})$ (top left), $|\text{EW}(\text{C II}^*)|$ and $|\text{EW}(\text{Si II}^*)|$ (top right), $R_f(\text{C II})$ and $R_f(\text{Si II})$ (bottom left), and $v_{\text{cen}}(\text{C II})$ and $v_{\text{cen}}(\text{Si II})$ (bottom right) for the 22,500 mock spectra in the simulations (small points) and the CLASSY observations (circles). The procedure used to derive each measurement is given in the text. Each point is color coded by its stellar mass (for the simulation points, it corresponds to the stellar mass of the simulation output used to construct the spectra). The dotted lines indicate the 1:1 relations. On the side of these panels, we show histograms presenting the 1D distribution of the measurements. Except for Si II^* , the simulated spectra properties overlap with 87% of the CLASSY sample.

within that range, and four objects have $v_{\text{cen}}(\text{Si II}) < -300 \text{ km s}^{-1}$. Despite a few CLASSY outliers having either larger EWs or v_{cen} values, the overlap between the ranges of the resonant line properties is remarkable.

Regarding the fluorescent emission properties (upper right panel), the range of $|\text{EW}(\text{C II}^*)|$ is between 0 and 1 for both samples. However, the simulated spectra typically have $|\text{EW}(\text{Si II}^*)|$ between 0.4 and 1.5 Å while CLASSY galaxies have $|\text{EW}(\text{Si II}^*)|$ between 0 and 0.6 Å. There are several possible factors that could explain the fact that we observe an overlap for $|\text{EW}(\text{C II}^*)|$ but not for $|\text{EW}(\text{Si II}^*)|$. First, one must keep in mind that the separation between the C II^* fluorescent and C II resonant wavelengths is small. Consequently, C II^* photons emitted close to the resonance (i.e., without a large velocity offset) could be reabsorbed in the resonant channel as they travel in the ISM. This makes the C II^* emission more difficult to interpret because it suggests that we only observe a certain fraction of the total C II^* emission that is produced. Second, these differences might also suggest that either the physics of the simulation or of our

radiative-transfer recipe cannot fully reproduce the fluorescent emission properties of the CLASSY objects. In particular, differences in the abundance ratios, assumed solar in this work, or in the number of ions populating the fine-structure level for C^+ and Si^+ , would lead to a different $\text{EW}(\text{C II}^*)$ to $\text{EW}(\text{Si II}^*)$ relation. M21 also demonstrate that the turbulent velocity and/or dust opacity model can considerably influence the shape and properties of the fluorescent emission. Finally, aperture losses also largely affect the observed C II^* and Si II^* emission, and their impact may vary for C II^* and Si II^* . We discuss this latter aspect in Section 4, and a separate analysis, focused on the simulation and its post-processing will further investigate the physical mechanisms that can further explain the strength of the fluorescent emission in the simulated spectra.

3.1.2. Si II versus C II

Figure 4 also reveals some interesting trends connecting the resonant C II and Si II properties. In the simulated spectra, $\text{EW}(\text{C II}) < \text{EW}(\text{Si II})$ for weak absorption lines ($\text{EWs} < 1 \text{ \AA}$),

and $v_{\text{cen}}(\text{C II})$ more negative (positive) than $v_{\text{cen}}(\text{Si II})$ for blueshifted (redshifted) absorption lines. These trends can be explained by the impact of the $\text{C II}^* \lambda 1335$ features on the $\text{C II} \lambda 1334$ absorption line. Spectra with significant C II^* fluorescent emission will have lower $\text{EW}(\text{C II})$, and more negative $v_{\text{cen}}(\text{C II} \lambda 1334)$ because the emission component fills a significant portion of the absorption line. On the other hand, spectra with broad $\text{C II} \lambda 1334$ absorption lines also exhibit a significant absorption component at the fluorescent wavelength. The combined resonant and fluorescent absorption feature yields larger $\text{EW}(\text{C II})$ and more positive $v_{\text{cen}}(\text{C II})$ compared to Si II .

The lower left panel of Figure 4 shows that $R_f(\text{C II})$ is typically larger than $R_f(\text{Si II})$ in the simulation. This is because the $\text{C II} \lambda 1334$ lines are typically more affected by infilling due to resonant scattering than the $\text{Si II} \lambda 1260$ lines.

It is interesting to note that the CLASSY measurements exhibit slightly different behaviors compared to the simulated data. In particular, we find that the CLASSY objects typically have $\text{EW}(\text{Si II}) > \text{EW}(\text{C II})$, $v_{\text{cen}}(\text{Si II}) > v_{\text{cen}}(\text{C II})$, and $R_f(\text{C II}) \approx R_f(\text{Si II})$. The two former trends can be explained by the presence of the $\text{S II} \lambda 1259$ absorption line blended with the $\text{Si II} \lambda 1260$ line, which is not modeled in the simulated spectra. This additional absorption on the blue side of the Si II line biases the EW and v_{cen} measurements toward larger and lower values, respectively. Appendix A presents examples of spectra that clearly highlight the impact of the S II absorption line.

Still, the impact of the S II absorption line cannot explain why the CLASSY spectra have $R_f(\text{C II}) \approx R_f(\text{Si II})$ while the simulated spectra yield $R_f(\text{C II}) \geq R_f(\text{Si II})$. Interestingly, residual flux discrepancies between different ions (or different transitions of the same ion) have been highlighted in several observational works that also found evidence that the LIS absorption lines were saturated (Reddy et al. 2016; Gazagnes et al. 2018; Du et al. 2021; Saldana-Lopez et al. 2022). In general, we expect low-ionized metallic ions to coexist within the same gas phase, hence to have the same residual flux assuming the transitions are saturated. Yet, the C II ionization potential is slightly higher than Si II , such that it can have a higher contribution from the ionized gas. The different causes of the residual flux disparities can either be differences in the saturation of the transition, in the amount of infilling due to resonant scattering, or also systematic differences in the ionized and neutral fractions, or Si to C abundances between the CLASSY galaxies and the simulation. In Section 5.2, we explore the spatial distribution of the residual flux and discuss further the most probable origin of this discrepancy.

Finally, we note that the CLASSY fluorescent EW values are scattered around the 1:1 line, while $\text{EW}(\text{Si II}^*) > \text{EW}(\text{C II}^*)$ in the simulation. We refer the reader to Section 3.1.1 for the discussion of the different factors that can explain the discrepancy between the Si II^* and C II^* emission in the simulation. Additionally, we further highlight in Section 4 that the fluorescent emission observed in CLASSY is affected by aperture losses, so the comparison of both trends must be considered carefully.

The joint comparison of the Si II versus C II properties highlights several differences in the trends observed in the simulation and in the observations, some of which can be explained by the caveats of our measurement approach, while others, related to, e.g., the residual flux or the strength of the Si II^* emission, are further discussed in Sections 4 and 5.2 in the

context of aperture loss. Overall, only six out of 45 CLASSY galaxies have spectral properties (in particular, their absorption line EWs and central velocities) that are clearly not replicated in the simulation, with five of these objects having M_* larger than the simulated galaxy. Hence, the significant overlap between simulated and observed line properties is extremely promising as it highlights the potential of RHD/RT simulations in replicating the environment of real star-forming galaxies and producing diverse and physically realistic spectra which compare to observations. We further explore this point in the next section.

3.2. Finding the Best Matches for Each CLASSY Objects

In this section, we directly compare the C II and Si II line profiles of the 45 CLASSY galaxies to the spectra generated using the simulation. In particular, for each CLASSY object, we look for the mock spectrum that best matches the observed profiles. We implement a simple minimization procedure, which is performed as follows: the mock and observed spectra are normalized using the median of the flux in a feature-free interval around 1256 and 1331 Å, respectively. Then, for each observed spectrum, the 22,500 mock spectra are degraded to the resolution of the observation using a Gaussian line spread profile, in which FWHM is fixed to the value reported in Table 3 in Berg et al. (2022). We then determine which mock spectrum best minimizes the equation

$$\begin{aligned} \tilde{\chi}^2 &= \frac{\chi_{\text{C II}}^2 + \chi_{\text{Si II}}^2}{n_{\text{C II}}^{\text{obs}} + n_{\text{Si II}}^{\text{obs}}}, \text{ where} \\ \chi_{\text{C II}}^2 &= \sum \left(\frac{f_{\text{C II}}^{\text{obs}} - f_{\text{C II}}^{\text{sim}}}{\sigma_{\text{C II}}^{\text{obs}}} \right)^2 \text{ and} \\ \chi_{\text{Si II}}^2 &= \sum \left(\frac{f_{\text{Si II}}^{\text{obs}} - f_{\text{Si II}}^{\text{sim}}}{\sigma_{\text{Si II}}^{\text{obs}}} \right)^2. \end{aligned} \quad (2)$$

Here, $f_{\text{ion}}^{\text{obs}}$ and $f_{\text{ion}}^{\text{sim}}$ are the observed and simulated flux in the wavelength regions of each ion, respectively, $\sigma_{\text{ion}}^{\text{obs}}$ is the error on the observed flux, and $n_{\text{ion}}^{\text{obs}}$ is the number of bins in the spectrum of each ion. If the wavelength range around Si II or C II is not observed, the corresponding χ^2 and n^{obs} are set to 0. We mask all the Milky Way absorption and emission lines falling within each spectrum. Regarding the S II absorption line at 1259.52 Å, which contribution is not modeled in the mock spectra, we choose to mask a region of $\pm 100 \text{ km s}^{-1}$ around it only if it is clearly resolved.

We compute $\tilde{\chi}^2$ using an interval from -800 to 700 km s^{-1} for $\text{C II} \lambda 1334$ and from -800 to 1500 km s^{-1} for $\text{Si II} \lambda 1260$. We tested different interval sizes and found that it does not impact the results if the full extent of the absorption and emission features is included for both lines. We also compute a $\tilde{\chi}_{\text{abs}}^2$ and $\tilde{\chi}_{\text{fluo}}^2$ to provide insights into the fit quality around the absorption and fluorescent features, respectively. $\tilde{\chi}_{\text{abs}}^2$ is derived using an interval of $\pm 200 \text{ km s}^{-1}$ around the velocity at the minimum depth of the C II and Si II absorption lines. $\tilde{\chi}_{\text{fluo}}^2$ is derived using an interval of $\pm 200 \text{ km s}^{-1}$ around the C II and Si II fluorescent transition wavelength.

Figure 5 presents the matching results for three galaxies, J1428+1653, J0337-0502 (also known as SBS 0335-052E) and J1612+0817, and Appendix B.1 shows the matching results for all CLASSY objects. We select these galaxies as examples

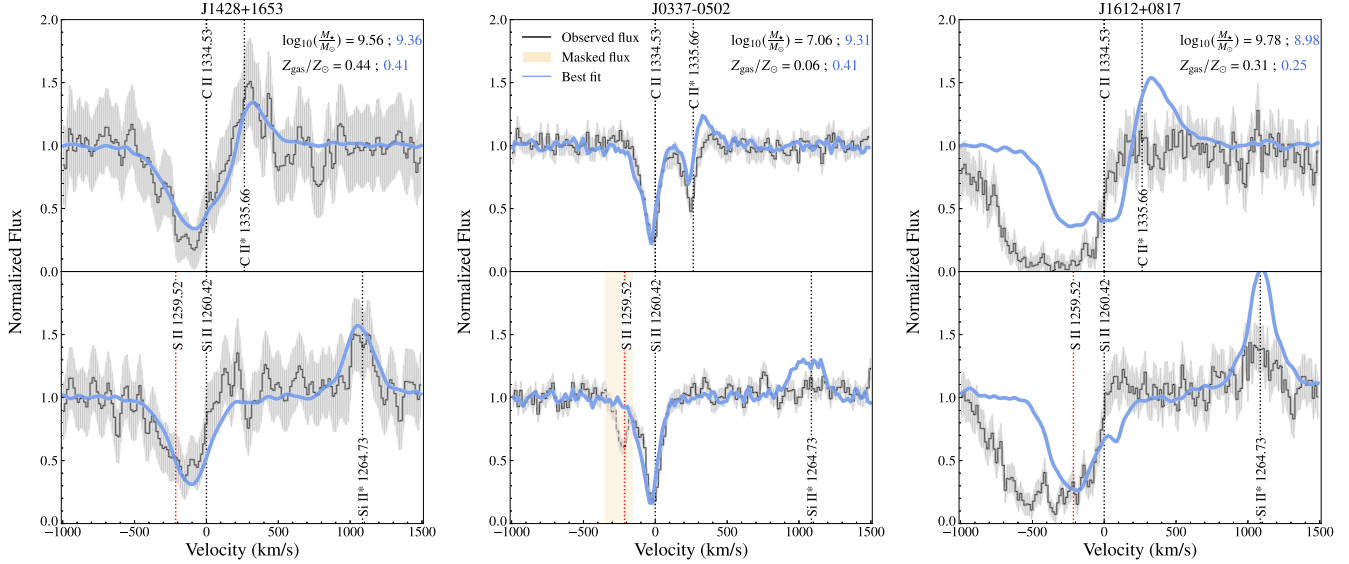


Figure 5. The best-matching spectrum of the C II $\lambda 1334 + \text{C II}^* \lambda 1335$ (top panels) and Si II $\lambda 1260 + \text{Si II}^* \lambda 1265$ (bottom panels) line profiles for three CLASSY galaxies (J1428+1653 left, J0337-0502 middle, and J1612+0817 right) using the procedure detailed in Section 3.2. The black line represents the observed flux, the gray shaded area denotes the flux error, the vertical dotted lines indicate the expected location of each transition, the yellow shaded area shows masked regions, and the gray shaded area the flux error. We only mask the wavelength region around S II 1259 Å when it is clearly resolved (e.g., only in the middle panel here). The blue line indicates the mock spectrum that best matches the observation. In the top right corner of the top panels, we detail the stellar mass and gas metallicity of the CLASSY galaxy (in black) and of the virtual galaxy at the time step where the best fit has been found (in blue). The best-matched spectrum of J1428+1653 accurately reproduces both the absorption and fluorescent emission, and similar matching results are found for 28 CLASSY galaxies in total. The best-matched spectrum of J0337-0502 matches the resonant absorption well but overestimates the fluorescent emission. We observe a similar discrepancy for nine CLASSY galaxies. The best-matched spectrum of J1612+0817 fails to reproduce both the absorption and emission features. We find that the spectra of seven CLASSY galaxies are poorly matched, and five of them (including J1612+0817) have a stellar mass larger than the simulated galaxy. Appendix B.1 presents the plots for all 45 CLASSY galaxies.

because (i) they have different absorption and emission line morphologies, suggesting that they have distinct ISM properties, and (ii) they are representative of the level of agreement between best-matched mocks and CLASSY spectra over the whole sample. The J0337-0502 spectrum shows narrow, relatively symmetric lines, and lacks fluorescent emission with C II* seen in absorption. The spectrum of J1429+0643 shows broad, asymmetric C II and Si II absorption lines and relatively significant C II* and Si II* emission. Finally, the spectrum of J1612+0817 presents broad, blueshifted absorption features for both Si II and C II with little fluorescent emission. Importantly, J1612+0817 has a stellar mass of $10^{9.78} M_\odot$, larger than the simulated galaxy. Both its EW(C II) and EW(Si II) values are outside the range seen in the simulation (see Section 3) so we do not expect to find a good match for this object.

Figure 5 highlights that the best-matching spectrum of J1428+1653 reproduces well the C II and Si II line profiles ($\tilde{\chi}^2_{\text{abs}}$ and $\tilde{\chi}^2_{\text{fluo}} < 1.5$), and we find similar matching results for 28 CLASSY galaxies. The best-matching spectrum of J0337-0502 matches the absorption lines well but overpredicts the observed fluorescent features around both lines ($\tilde{\chi}^2_{\text{fluo}} > 1.5$). Eight other spectra present the same discrepancy. Finally, the best-matching spectrum of J1612+0817 fails to reproduce both the absorption and fluorescent features ($\tilde{\chi}^2 > 3$). In total, we find that the spectra of seven galaxies (J0808+3948, J1112+5523, J1144+4012, J1157+3220, J1416+1223, J1525+0757, J1612+0817) are poorly matched, and five of these objects (J1112+5523, J1144+4012, J1416+1223, J1525+0757, J1612+0817) have M_* larger than the simulated galaxy. For the two remaining galaxies, J0808+3948 and J1157+3220, the absorption lines are significantly blueshifted, and such profiles are not well replicated in our simulation.

Over the whole sample, we find that the median $\tilde{\chi}^2$ is 0.84, the median $\tilde{\chi}^2_{\text{abs}} = 0.82$ and the median $\tilde{\chi}^2_{\text{fluo}} = 1.37$. In general, the simulated spectrum matches the resonant absorption well but sometimes significantly misrepresents the observed fluorescent emission. This discrepancy is typically larger for Si II* than for C II*, which one might expect given the results shown in Section 3. In the next section, we show how aperture losses can explain the lack of fluorescent emission observed in some CLASSY spectra.

Overall, the ability to reproduce such a diversity of LIS spectra with a single simulated galaxy of $M_* \sim 10^9 M_\odot$ is remarkable. While the spectra of higher mass galaxies are not well matched, we do not find a significant variation of the median $\tilde{\chi}^2$ for galaxies with $M_* < 10^9 M_\odot$. This suggests that the simulated spectra reproduce equally well the spectra of CLASSY galaxies less or equally massive than the virtual galaxy. This might be surprising given the expected tight relations between stellar mass and the LIS line properties (e.g., Alexandroff et al. 2015; Heckman et al. 2015; Chisholm et al. 2017a) and we explore this aspect further in Section 5.1.

4. Aperture Loss Effects on the Fluorescent Emission

In recent years, several studies have explored the emission properties of LIS metal lines using different approaches such as Monte Carlo methods in idealized geometries (Prochaska et al. 2011), semi-analytic computations (Scarlata & Panagia 2015; Carr et al. 2018; Carr & Scarlata 2022), or zoom-in simulation post-processed with radiative-transfer techniques (Mauerhofer et al. 2021). These different approaches all emphasized that several factors, including dust extinction, gas densities, or outflow geometry (the latter aspect is also discussed in Jaskot & Oey 2014; Rivera-Thorsen et al. 2015) regulate the shape of the absorption and fluorescent emission profiles. These works, and

most if not all observational papers studying fluorescent emission (Shapley et al. 2003; Erb et al. 2010, 2012; Finley et al. 2017a, 2017b; Steidel et al. 2018; Wang et al. 2020), also mention the impact of aperture loss, which must be carefully considered if one aims to tie together simulations and observations.

The aperture size has a strong influence on the observed emission because the spatial extent of the fluorescent emission is larger than for the UV continuum. If the gas extent of the galaxy is significantly larger than the spectrograph aperture size (which sometimes also includes several star clusters), one will capture only a disproportional fraction of the fluorescent emission. Several studies have shown how aperture loss might explain the absence or weakness of the fluorescent lines in certain observations (e.g., Shapley et al. 2003; Schwartz et al. 2006; Scarlata & Panagia 2015). Given the relatively low redshifts and larger apparent sizes of the CLASSY galaxies ($z = 0.002\text{--}0.182$) and the limited size of the COS aperture ($2.\overset{\prime}{5}$), these effects might also justify the lack of fluorescent emission in several CLASSY spectra. In Section 4.1, we explore the connection between the aperture sizes and the C II* and Si II* features in CLASSY and in the simulated spectra. Section 4.2 expands the analysis of the best-matching mock spectra by including the constraints of the COS aperture.

4.1. Clues from Observations and Simulations

We first explore the impact of aperture size on the CLASSY spectra. Arellano-Córdova et al. (2022) thoroughly investigated how aperture size affects nebular properties derived from optical spectra of the CLASSY sample and found it has a negligible impact on the derived measurements. Their work focuses on properties inferred from ratios of nebular lines such that the absence of significant differences is not unexpected. Here, we are directly looking at (partially) resonant lines and their properties. The latter depends on the spatial extent of the gas phases and their geometry, such that one expects aperture losses to play a much more critical role. To confirm this hypothesis, we explore the relationship between the EW of the observed fluorescent emission as a function of the galaxy size which we estimate using its optical half-light radius (r_{50}^{opt} , estimated from the u band, see Table 6 from Berg et al. 2022).

Figure 6 shows the CLASSY $|\text{EW}(\text{C II}^*)|$ and $|\text{EW}(\text{Si II}^*)|$ as a function of $r_{\text{cos}}/r_{50}^{\text{opt}}$, where r_{cos} is the radius of the COS aperture, or $1.\overset{\prime}{25}$. The $r_{\text{cos}}/r_{50}^{\text{opt}}$ ratio provides insights into the fraction of galaxy optical flux that falls within the COS aperture. For example, a ratio of 1 indicates that $\sim 50\%$ of the total optical flux fell within the COS aperture, and larger (lower) values suggest that more (less) light has been captured.

The comparison of the optical size to the properties of UV lines suffers some caveats. Indeed, the UV light of the CLASSY sample is dominated by young stars and so is sometimes more spatially compact than the optical light. This may mean that a higher fraction of the UV light was actually captured within the COS aperture than assumed here. The UV half-light radii are sometimes estimated using the near-UV COS acquisition images, but the COS aperture vignettes the light it collects (the light at the edges of the aperture has a lower transmission than at the center), resulting in potentially artificially smaller half-light radii. Hence, in the current work, we only use r_{50}^{opt} as a tracer of the galaxy size.

Figure 6 highlights that almost all galaxies with $\text{EWs} \gtrsim 0.3$ Å have $r_{\text{cos}}/r_{50}^{\text{opt}} > 1.0$, and the CLASSY spectra with the largest

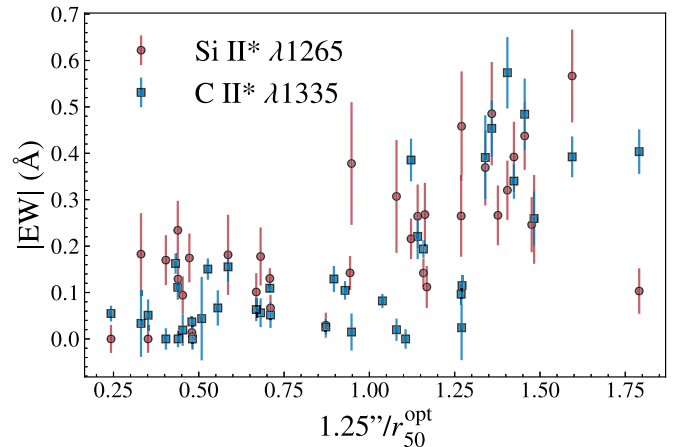


Figure 6. The measured $|\text{EW}(\text{C II}^*)|$ (blue) and $|\text{EW}(\text{Si II}^*)|$ (red) as a function of $1.\overset{\prime}{25}/r_{50}^{\text{opt}}$ ($1.\overset{\prime}{25}$ being the COS aperture radius) for the CLASSY observations. Galaxies with the largest EWs have the largest $1.\overset{\prime}{25}/r_{50}^{\text{opt}}$ values, with the exception of J1323-0132 (see discussion in the text).

EW(C II*) and EW(Si II*) have the largest $1.\overset{\prime}{25}/r_{50}^{\text{opt}}$ ratios, with the exception of J1323-0132. For this galaxy, we do not detect any C II or Si II absorption, suggesting that this galaxy is largely depleted of low-ionized metal gas and therefore explains the relative weakness of the fluorescent features. These results support that several CLASSY spectra may miss a significant part of fluorescent emission due to aperture losses.

We now investigate how mimicking aperture loss in the simulation impacts the C II* and Si II* properties of the mock spectra. In Section 3, the mock spectra were extracted using a circular fiducial aperture of $1''$ diameter, which encompasses the galaxy full extent at $z = 3$. To investigate the impact of varying the aperture size, we use a single simulation output of the galaxy at $t = 2$ Gyr for which we compute integral field unit cubes for each of the 300 lines of sight. Each cube consists of 4096 individual spectra corresponding to the 64×64 spatial pixels. The pixel physical size is 120×120 pc, such that the entire cube face is $\sim 7.7 \times 7.7$ kpc.

For each of the 300 directions, we extract integrated C II and Si II spectra using circular apertures of increasing radius, using a one-pixel step, centered on the brightest pixel. We then measure $\text{EW}(\text{C II}^*)$ and $\text{EW}(\text{Si II}^*)$ in each spectrum and measure for each ion the evolution of $\text{EW}(r)/\text{EW}_{\text{total}}$, where $\text{EW}(r)$ is the measurement at a given radius, and EW_{total} is the total EW obtained by integrating the entire cube face. The $\text{EW}(r)/\text{EW}_{\text{total}}$ ratio provides insights into the fraction of the total fluorescent flux which is captured as a function of the aperture size.

Figure 7 presents the C II* and Si II* $\text{EW}(r)/\text{EW}_{\text{total}}$ profiles derived over the 300 lines-of-sight measurements, as a function of radii. Using an image of the virtual galaxy in the optical (at 3500 Å), we also measure the r_{50}^{opt} of the virtual galaxy (see Appendix C) to better compare the results from the simulation with the analysis done for the CLASSY spectra in Figure 6.

The gradual increase of $\text{EW}(\text{C II}^*)$ and $\text{EW}(\text{Si II}^*)$ with radii demonstrates that the size of the aperture critically impacts the strength of the fluorescent emission observed in the simulated spectra. We note that the Si II* $\text{EW}(r)/\text{EW}_{\text{total}}$ has a steeper increase with r , and the typical variations around the median are smaller compared to C II*. This is because the C II fluorescent emission is blended with the resonant absorption so that the C II* emission strength also depends on the absorbing gas properties along the line of sight.

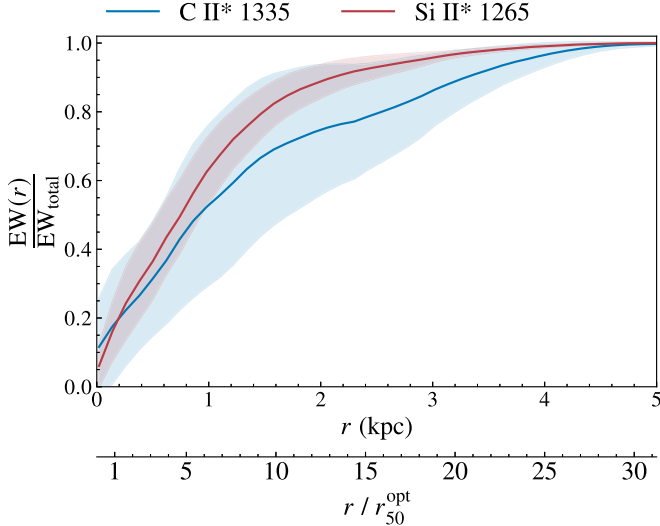


Figure 7. The evolution of the $\text{EW}(r)/\text{EW}_{\text{total}}$ for $\text{C II}^* \lambda 1335$ (blue) and $\text{Si II}^* \lambda 1265$ (red) as a function of the aperture radius (r) for the simulated galaxy. The solid lines and shaded areas denote the median and standard deviation over 300 lines of sight, respectively, using a single simulation output of the galaxy at $t = 2$ Gyr. The bottom x-axis shows the ratio between r and r_{50}^{opt} for the virtual galaxy. Simulated spectra with $r < r_{50}^{\text{opt}}$ typically exhibit little to no fluorescent emission. r must be at least ~ 20 and 25 times larger than r_{50}^{opt} if one aims to capture all the fluorescent emission for Si II^* and C II^* , respectively.

In general, Figure 7 highlights that little fluorescent emission is observed in mock spectra extracted using apertures with $r < r_{50}^{\text{opt}}$, which is consistent from the analysis of Figure 6. Furthermore, this figure suggests that the aperture size must be 5 times larger than r_{50}^{opt} to capture at least 50% of the total fluorescent emission for both ions, and ~ 20 and 25 times larger if one aims to capture all of the Si II^* and C II^* emission, respectively.

While Figure 6 indicates that all CLASSY galaxies have $r/r_{50}^{\text{opt}} < 2$, Figure 7 indicates that we should capture at best 20% of the total flux. If this was correct, large discrepancies between the simulated and observed fluorescent emission should be seen for the whole sample, yet, we showed in Section 3.2 that this is only the case for a few (eight) objects. This inconsistency can be explained by several factors. First, in the simulation, both $\text{EW}(r)/\text{EW}_{\text{total}}$ and the measured r_{50}^{opt} varies as a function of the viewing angle (see the error bar on the median r_{50}^{opt} derived in Appendix C) and as a function of the time step considered (and hence of the galaxy property at these ages). Second, the CLASSY galaxies present diverse sizes and morphologies (see, e.g., Figure 2 in Berg et al. 2022) which might not resemble the simulated galaxy. In particular, several objects seem to present several bright star clusters within the COS aperture, while most of the observed continuum flux in the simulation emerges from a single star cluster (see Section 5.2). This means that the spatial extent of fluorescent emission in the simulation might strongly differ from these observations, and a relatively lower r/r_{50}^{opt} ratio could already capture most of the total fluorescent flux. Hence, because Figure 7 builds upon a single virtual object, the comparison of the scaling relations in the simulation with the CLASSY measurements should be taken with caution.

Despite these caveats, Figures 6 and 7 present trends that clearly highlight the importance of constraining aperture losses for analyzing fluorescent emission observations. In the next

section, we refit some of the CLASSY spectra using an approach that accounts for the COS aperture size.

4.2. Improving the Matches Using Aperture Constraints

Some of the best-matched mock spectra found in Section 3.2 present fluorescent emission features which exceed the flux observed in the CLASSY spectra. Section 4.1 highlighted that aperture effects could be the predominant cause of this discrepancy. In this section, we refine the fitting procedure detailed in Section 3.2 to explore whether we can improve the matches if we account for aperture effects. For this experiment, we use the simulation output described in Section 4.1 (300, 64×64 pixels images of the simulated galaxy at $t = 2$ Gyr). For each CLASSY spectrum to be matched, we fix the size of the aperture in the simulation to the size of the COS aperture at the galaxy redshift. Then, for each direction, we extract the Si II and C II spectra for all regions in which the central pixel luminosity is at least 50% of the brightest pixel for this direction. This strategy ensures that we follow a procedure consistent with the CLASSY HST/COS acquisition method, which automatically centers its aperture on the brightest region.

Here, we use a single simulation output at $t = 2$ Gyr, while we used 75 different time steps in Section 3.2. This is because the production of spectral data cubes is computationally expensive. Fortunately, the output at $t = 2$ Gyr is best situated to analyze the CLASSY observations: most (21 out of 45) of the best-matched mock spectra found in Section 3.2 originate from this time step. This output corresponds to the time step A in M21.

We use the *aperture-based* procedure described above to fit 14 CLASSY galaxies that have (i) $r_{50}/1.25 > 1$ (i.e., the galaxies most affected by aperture losses), (ii) observations for both Si II and C II , enabling us to assess both LIS lines simultaneously, and (iii) had their best match found in the simulation output at $t = 2$ Gyr. We compare in Figure 8 the C II and Si II matches obtained using the approach in Section 3.2 (referred to as *all-flux fits*) and the fits obtained using the new approach detailed in this section (referred to as *aperture-based fits*) for J0337-0502 and J1225+6109. Appendix B.2 shows this comparison for all 14 galaxies.

For both J0337-0502 and J1225+6109, the aperture-based fits better replicate the multicomponent profile. For J0337-0502, the fluorescent feature fits are significantly improved, while the quality of the resonant absorption fits remains unchanged. For J1225+6109, the best-matched mock spectrum for J1225+6109 better replicates the absorption features for both lines, the C II^* absorption is also better matched, but, interestingly, the all-flux match seems to better reproduce the absorption around Si II^* . Observing absorption around the fluorescent wavelength suggests that the overall gas is too opaque on this line of sight such that fluorescent photons emitted in that direction are either absorbed or scattered back in different directions where they can escape. This absorption would emerge from thick regions, located close to and around the brightest stars. For this galaxy, the COS-based aperture radius is only 2 pixels wide such that it is not large enough to capture these regions. Overall, this narrow absorption feature is relatively weak, within 1.5σ of the flux error, so the differences between both fits are not significant.

To quantify the global improvements enabled by the aperture-based approach, we look at the evolution of the best match $\tilde{\chi}^2$, $\tilde{\chi}_{\text{abs}}^2$, and $\tilde{\chi}_{\text{fluo}}^2$ in Figure 9. We define a difference of 1 in the average $\tilde{\chi}^2$ as a significant improvement or deterioration of the fit quality (i.e., the deviation to the observation increases/decreases by 1σ on average). The

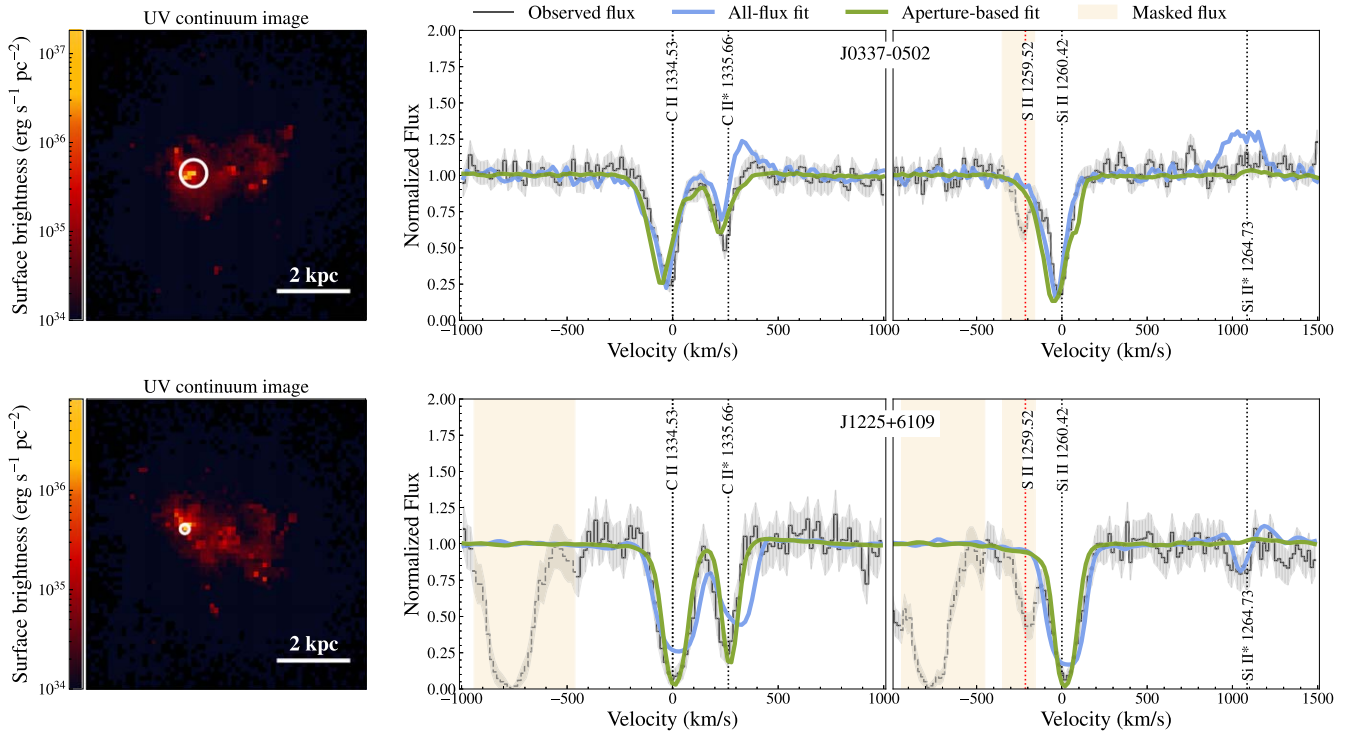


Figure 8. The fitting results based on the aperture-based approach described in Section 4.2 for two CLASSY galaxies (J0337-0502 top row and J1225+6109 bottom row). The left panel presents an image of the simulated galaxy in the direction where the best mock spectrum has been found. The white circle shows the fiducial aperture used to extract the spectra, centered on the brightest pixel in the region. The size of this region corresponds to the size of the COS aperture at the galaxy redshift. The right panels present the comparison of the previous best-matched mock spectra shown in Section 3.2 (referred to as all-flux fit) and the new aperture-based fits. The aperture-based fits reproduce better the line profiles around the C II* and Si II* fluorescent channels, emphasizing that aperture effects play a critical role in the analysis of the fluorescent emission in the CLASSY galaxies.

evolution of the χ^2 values highlights that the aperture-based fits improve the overall fit quality for three of 14 galaxies, while no significant changes are found for the other spectra.

Most notably, we find significant improvements of the $\tilde{\chi}^2_{\text{fluo}}$ for eight galaxies, with two galaxies improved by a factor larger than 5, and no substantial changes for five objects. Four of these five objects already had good matches as shown by their low $\tilde{\chi}^2_{\text{fluo}}$ values. Hence, using a smaller aperture does not impact the good fits.

Finally, when considering the reduced $\tilde{\chi}^2_{\text{abs}}$ values, we only find significant improvements for two galaxies. For one of these, J1525+0757 ($r_{50} \sim 1.^{\prime\prime}32$), the best-matched mock still poorly matches the observed spectrum. This galaxy is one of the high-mass objects, and its spectrum exhibits very large absorption lines, which none of the available mock spectra can reproduce. This suggests that accounting for aperture losses does not improve the fit quality for the CLASSY galaxies with M_* larger than the virtual galaxy.

Overall, the approach that mimics the aperture effects for the CLASSY objects enables us to significantly improve the results of Section 3.2 by extracting mock spectra that better match the CLASSY fluorescent features. This indicates that aperture-biased observations limit the interpretation of fluorescent line spectra because they underestimate the strength of the fluorescent emission. On the other hand, aperture losses may have a lesser impact on the properties and shape of the resonant absorption features. This is because the latter is predominantly produced from the gas around the brightest stars, and is likely affected by the ratio between the angular size of the continuum source and the instrument aperture. We discuss this aspect further in Section 5.2.

5. Discussion

Here, we discuss the outcomes of Sections 3 and 4. Section 5.1 discusses the origin of the diversity of the LIS metal line profiles that can be produced using a single simulated galaxy. In Section 5.2, we use the simulation to explore the physical and spatial origin of the different spectral features that compose a LIS metal line spectrum.

5.1. The Feasibility of Using a Single-Galaxy Simulation to Interpret a Range of Physical Conditions

Sections 3.2 and 4.2 highlighted that the mock profiles generated in this work provide accurate replicates of the HST/COS observations of 38 CLASSY galaxies with a broad range of stellar masses (10^6 – $10^9 M_\odot$) and metallicities (0.02–0.55 Z_\odot). The ability to trace such a diversity of galaxy environments using a single simulated object at $z \sim 3$ with limited stellar mass (7.1×10^8 to $2.3 \times 10^9 M_\odot$) and metallicity variations (0.24–0.43 Z_\odot) is remarkable. In particular, it supports that the observation of a certain line profile is mostly determined by the ISM properties (geometry, densities, and kinematics) along the line of sight. Yet, this result might come as surprising since one expects the LIS line properties to be tightly connected to galaxy properties such as stellar mass or metallicity (e.g., Alexandroff et al. 2015; Heckman et al. 2015; Chisholm et al. 2017a; Xu et al. 2022, 2023). In this section, we examine the origin of the diversity of LIS line spectra that can be produced using a single galaxy.

In Figure 10, we compare the variation of the EW(Si II) and $-v_{\text{cen}}(\text{Si II})$ properties to the variation of the galaxy SFR over the 75 time steps (690 Myr). Note that we use the Si II properties because, for C II, the contributions of the resonant

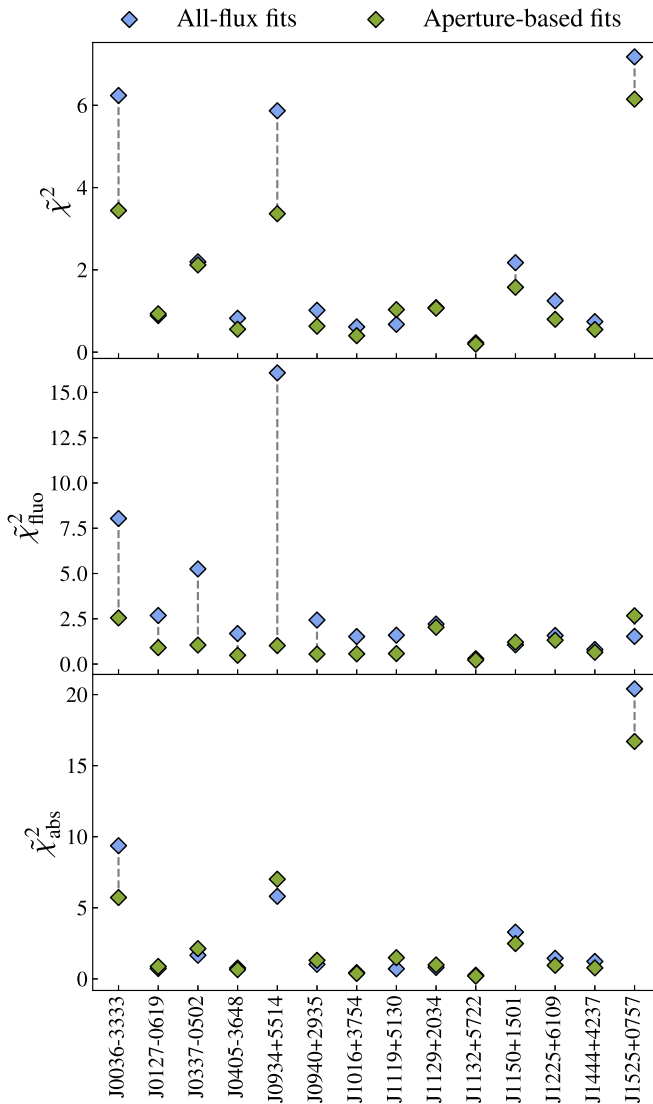


Figure 9. The comparison of the χ^2 values for the all-flux fits (shown in Section 3.2) and the aperture-based fits for the 14 CLASSY galaxies rematched in Section 4.2. The top panel presents the evolution of the $\tilde{\chi}^2$ values derived using Equation (2). The middle and bottom panels show the evolution of the $\tilde{\chi}^2_{\text{fluo}}$ and $\tilde{\chi}^2_{\text{abs}}$ values, respectively. Most notably, the aperture-based approach enables significant improvements of the $\tilde{\chi}^2_{\text{fluo}}$ for eight galaxies, emphasizing that we need to account for aperture losses when comparing the fluorescent emission properties in simulations and observations. On the other hand, aperture losses may have a lesser impact on the properties and shape of the resonant absorption feature.

absorption and fluorescent emission features are often blended, complicating their analysis.

Figure 10 highlights that the evolution of $-v_{\text{cen}}(\text{Si II})$ is tightly related to the temporal variations of the SFR (Kendall-tau correlation coefficient of 0.67, p -value of 4.92×10^{-13}). We find spectra with blueshifted absorption lines (suggesting dominant outflows) in time ranges where the galaxy experiences intense star formation bursts (around 1.6 and 2 Gyr). We observe a slight offset between the gas kinematics traced by $-v_{\text{cen}}$ and the SFR. This behavior was already discussed in e.g., Trebitsch et al. (2017), Rosdahl et al. (2018) and indicates that outflows happen a short time after the SFR peak.

On the other hand, between bursts, the virtual galaxy experiences a period of relative quiescence (we note that it is

not entirely quiescent as it still forms stars). During that period, the typical Si II spectra exhibit absorption lines close to the systemic velocity or redshifted, suggesting the gas might be relatively static or with potential inflows.

While we observe a decrease in the median EW(Si II) values close to SFR peaks, the temporal evolution of EW(Si II) is less tightly related to the SFR than v_{cen} (Kendall-tau correlation coefficient of 0.01, p -value of 0.92), suggesting that other aspects must be accounted for to understand its decline through time. Nevertheless, both the fluctuations of the EW and v_{cen} values during the 690 Myr period considered highlight that there exists a large variability of the Si II profile properties as a function of time.

In addition to the time-variability, we denote a significant line-of-sight variability of the Si II properties seen at each time step. This aspect is highlighted by the shaded areas in Figure 10, which shows the fluctuations of the EW(Si II) and $-v_{\text{cen}}(\text{Si II})$ values over the 300 orientations at each time step. This line-of-sight variability may suggest that there is a broad distribution of metal densities and gas kinematics over the entire ISM. This aspect has already been shown in M21, whose authors highlighted that there exist significant spatial fluctuations (up to a factor of 10) of the gas metallicity along different lines of sight. The Si II properties variations as a function of viewing angle emphasize that ISMs are complex heterogeneous environments.

The overall decrease of EW(Si II) through time and the tight connection between the galaxy SFR and $-v_{\text{cen}}(\text{Si II})$ might indicate that the physical processes involved during star formation bursts have a significant impact on the structure of the galaxy's ISM and CGM. In particular, the fragmentation of the ISM into dense star-forming clouds, plus the stellar and/or supernovae feedback triggered during or shortly after these events may significantly transform the ISM and introduce large fluctuations in the typical spectral properties observed through time and per viewing angle. Overall, this time- and line-of-sight variability likely explains how a single galaxy can produce such a diversity of spectra that are representative of galaxies of comparable or smaller masses.

These results may suggest that there only exists a limited dependence on, e.g., M_* and Z for observing specific LIS spectral properties. Nevertheless, we highlighted in Section 3.2 that the spectra of the CLASSY objects with M_* larger than the virtual galaxy are not well reproduced using this simulation. As already noted for the Ly α line by Blaizot et al. (2023), this indicates that this simulation cannot help us interpret the spectra of more massive objects because the latter might have too complex ISM environments. Additionally, the 1D histograms shown in Figure 4 (Section 3.1.1) highlight that the range of simulated LIS properties follows a normal distribution function, which means that there does exist a set of *typical* LIS properties for this $10^9 M_\odot$ virtual galaxy at $z \sim 3$. In particular, it also suggests that the good agreement between spectra from very low-mass CLASSY galaxies and the simulated spectra do not necessarily mean that the virtual galaxy (and its simulation physics) accurately depicts all these objects. It is possible that these spectra are rare in the simulation, arising from time steps where the SFR is low for the virtual galaxy but would be considered intense for these low-mass objects. Therefore, M_* and Z may still play an important role in understanding the typical LIS spectral properties observed in certain galaxy populations because the likelihood of observing certain spectra is determined by these parameters. To test this hypothesis, one could perform the same experiment done in this work building

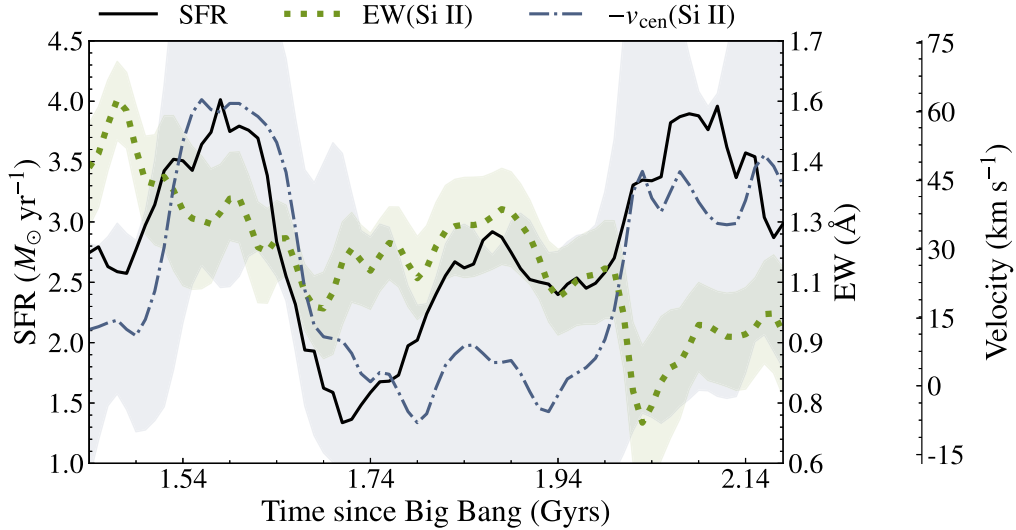


Figure 10. The evolution of the SFR of the galaxy in the zoom-in simulation over the time range of the outputs used to produce the mock C II and Si II line profiles (690 Myr). We show the evolution of the median EW(Si II) (green dotted line) and $-v_{\text{cen}}(\text{Si II})$ (blue dashed-dotted line) derived from the 300 line-of-sight measurements at each time step. The shaded areas represent the variation per output and is derived using the 16th and 84th percentiles of the 300 measurements. This figure highlights that both $-v_{\text{cen}}(\text{Si II})$ and EW(Si II) significantly vary as a function of time and as a function of the viewing angle. Additionally, the variations of $v_{\text{cen}}(\text{Si II})$ highlight that blueshifted absorption lines, suggesting the presence of outflows, are commonly found in spectra generated during star formation events. Overall, the variations of the LIS properties suggest that there exists a significant time and line-of-sight variability of the ISM/CGM properties, which can explain how a single galaxy can produce such a diversity of spectra.

upon virtual galaxies within a broader range of properties, using, e.g., satellite galaxies from the current simulations or galaxies from the SPHINX suite of cosmological RHD simulations (Rosdahl et al. 2018). In turn, the ability of lower and larger mass virtual galaxies in reproducing observations in the same regime will determine the exact influence of M_* on the LIS spectral properties. This effort, although necessary to constrain the range of spectral properties single-galaxy simulation can reproduce as a function of their properties, is beyond the current analysis.

5.2. Using the Simulation to Disentangle the Spatial Origin of the Spectral Features

This section uses the simulation to interpret the spatial and physical origin of the different spectral features (continuum emission, residual flux, or fluorescent emission) that compose LIS line spectra. We build upon the same data set we used in Section 4, which contains 64×64 images of the simulated galaxy in 300 directions at $t = 2$ Gyr. We explore the spatial properties of the Si II features²¹ in two directions corresponding to the lines of sight that provided the best-matched mock spectrum for the galaxies J0926+4427 and J0938+5428. These two galaxies show distinct line profiles: in J0926+4427, the Si II $\lambda 1260$ line exhibits a relatively narrow, blueshifted absorption with significant residual flux ($v_{\text{cen}} \approx -300 \text{ km s}^{-1}$ and $R_f \approx 0.5$). On the other hand, in J0938+5428, the line profile is broader, centered around the systemic velocity, and shows little residual flux ($R_f \sim 0.1$). Additionally, the EW of the fluorescent emission in J0926+4427 is typically 2 times larger than in J0938+5428. These line profile differences make these two galaxies optimal toy examples to investigate the origin of their spectral features using the simulation.

Figures 11 and 12 show images of the Si II continuum, fluorescence, and resonance surface brightness (SB) in the

orientation and time step that best matches the J0926+4427 and J0938+5428 spectra, respectively. Each panel presents the location of the brightest continuum pixel (yellow star), the contours enclosing 50% of the total flux (green lines), and the regions where dust attenuates by a factor of 2 or more the intrinsic emission (hash-dotted areas). We also construct maps representing the spatial distribution of $v_{\text{cen}}(\text{Si II})$ values per pixel. We show the Si II spectra extracted from (i) the brightest pixel, (ii) a circular aperture of radius 600 pc, (iii) a circular aperture of radius 1800 pc, and (iv) the whole image. We discuss below the origin of the stellar continuum, fluorescent emission, and residual flux contributions (bottom panels in each figure) in the two directions. To simplify the discussion, we refer to Figure 11 as the *J0926 direction* and to Figure 12 as the *J0938 direction*.

Stellar continuum: A single, compact region encompassing two and three pixels dominates half of the observed stellar continuum in the J0926 direction and in the J0938 direction, respectively. This region is more significantly attenuated by dust in the J0938 direction than in the J0926 direction. In both cases, the spectra extracted from the brightest continuum region exhibit fully covered absorption lines (no residual flux) and no fluorescent emission, indicating that the brightest stars are facing optically thick gas in these two directions. Additionally, in the J0926 direction, the absorption line in the brightest-region spectrum is significantly blueshifted (v_{cen} is $\leq -150 \text{ km s}^{-1}$), suggesting the presence of strong outflows.

Fluorescent emission: The fluorescent flux emerges from a larger region than the continuum in both directions, and the 50% contours either enclose regions with outflowing gas (the median v_{cen} values within the fluorescent contours are -150 and -30 km s^{-1} in the J0926 and J0938 directions, respectively), or with optically thin gas (i.e., the black pixels in the v_{cen} images, where no absorption lines are detected). Additionally, the fluorescent emission region is largely dust depleted in the J0926 direction, but not in the J0934 direction. This may explain why EW(Si II*) is 2 times larger in the J0926 direction than in the J0934 direction. Finally, the growth of the

²¹ We chose Si II because the resonant and fluorescent features are not blended, which simplifies the spatial analysis.

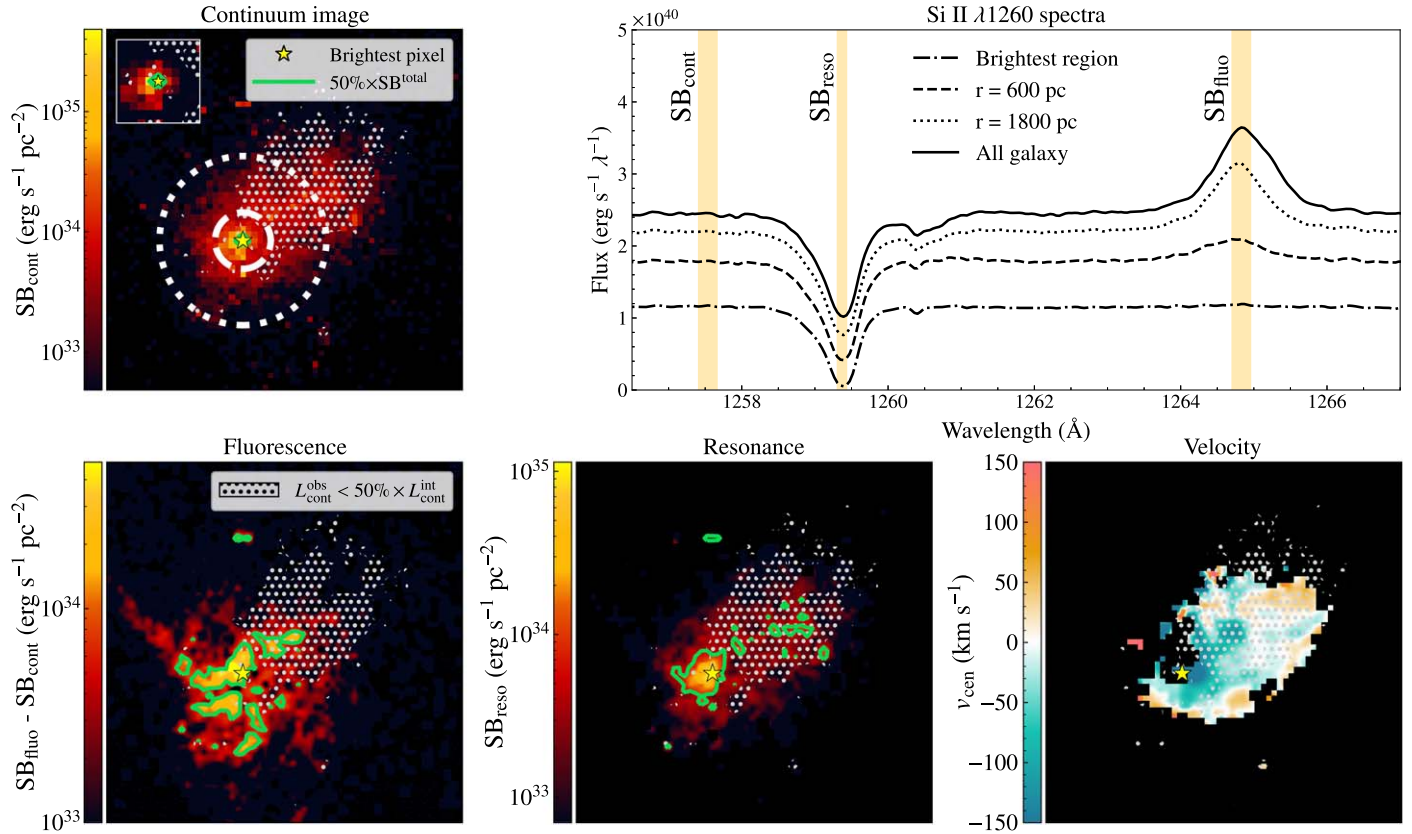


Figure 11. Si II images and spectra of the virtual galaxy for the line of sight that provides the best-matched mock spectrum for J0926+4427. The top left panel shows the integrated SB from the simulation corresponding to the continuum emission (SB_{cont}), and the bottom left and middle panels show the spatial distribution of the Si II fluorescence emission (measured on continuum-subtracted images, i.e., $SB_{\text{fluo}} - SB_{\text{cont}}$) and residual flux (SB_{reso} , measured in an interval around the absorption line maximal depth), respectively. In each of these images, a yellow star represents the brightest continuum pixel, green contour lines show the 50% level of the total SB, and the white hashed-dotted areas represent regions where the dust suppresses at least half of the intrinsic emission (the ratio of the observed and intrinsic luminosities is less than 0.5). The bottom right panel shows the distribution of v_{cen} values derived from the Si II spectrum in each pixel. Black pixels represent cases where the absorption component at 1260 Å is too faint or non-existent such that v_{cen} values cannot be robustly measured. All images are 64×64 pixels, with a pixel size of 120 pc. Finally, the top right panel presents the Si II spectra extracted based on (i) the brightest pixel (dotted-dashed line), (ii) a circular aperture of radius 600 pc (dashed), (iii) a circular aperture of radius 1800 pc (dotted line), and (iv) the entire image (solid line). The $r = 600$ and 1800 pc apertures are shown with matching line styles on the top left panel. The orange areas show the wavelength regions integrated to produce the continuum, fluorescence, and resonance images.

fluorescent emission in spectra extracted with increasing aperture radii highlights that most of the emission emerges from regions further away from the brightest stars, which is consistent with the analysis of Section 4.2.

Residual flux: We observe different spatial origins for the residual flux in the J0926 and J0938 directions. For J0926, it emerges from a relatively small and compact region surrounding the brightest stellar cluster. For the J0938 direction, it arises from an extended region further away from the brightest stars. In both directions, the 50% contours enclose pixels where we do not detect any absorption features, suggesting that some fraction of the residual flux comes from gas-depleted regions. Additionally, we find that the residual flux dominantly emerges from dust-depleted regions in both cases (87% and 92% of the pixels contributing to the residual flux are low-dust-attenuation regions for the J0926 and J0938 directions, respectively). The different spectra extracted in both directions highlight that we observe larger residual flux in spectra with increasing aperture radii, yet, the overall shape of the absorption line remains relatively unchanged. This has two important outcomes. First, aperture losses can also affect residual flux measurements and may explain why we observe different C II and Si II R_f trends in

the simulation and in the CLASSY sample (see Section 3.1.2). Second, the shape of the absorption line feature relates to the properties of the gas surrounding the brightest stars but provides little information about the gas properties in regions where the stellar continuum is strongly attenuated.

The analysis presented in this section paves the way for follow-up analyses that will further explore (i) the spatial properties of outflows and their impact on the ISM structure, and (ii) the origin of the trends that connect the LIS line residual flux and the escape of ionizing photons. In this work, for simplicity, we only consider two directions, which is already enough to highlight that the different spectral features (continuum emission, residual flux, fluorescent emission) have quite distinct spatial origins (little or no overlap in the 50% contours), which also vary as a function of the galaxy orientation. Importantly, this means that these different spectral features trace the properties of distinct regions in the galaxy’s ISM, which makes the interpretation of LIS line spectra complex and delicate. Nevertheless, such a high-resolution simulation provides an optimal laboratory to understand how these features relate to each other, which makes it a very promising framework for interpreting spectroscopic observations.

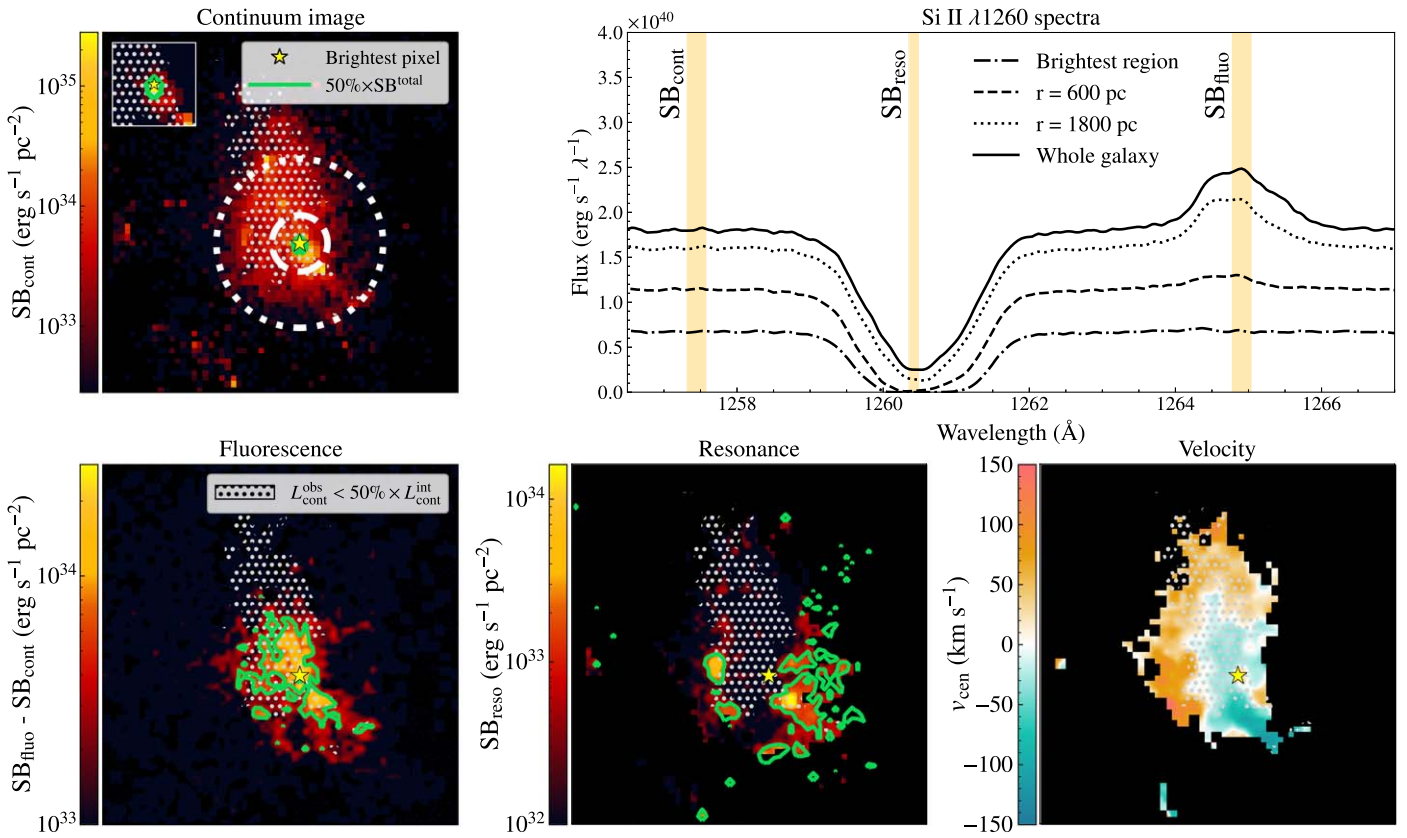


Figure 12. Same as Figure 11 for the line of sight that provides the best-matched mock spectrum for J0938+5428.

6. Conclusion

LIS absorption and emission lines provide crucial insights into the ISM of star-forming galaxies, but the complexity of the emerging line profiles makes their interpretation difficult. Building upon the work of Mauerhofer et al. (2021), we used radiative transfer post-processing of a $\sim 10^9 M_\odot$ dwarf galaxy in a zoom-in RHD simulation to create 22,500 C II $\lambda 1334$ +C II* $\lambda 1335$ and Si II $\lambda 1260$ +Si II* $\lambda 1265$ spectra (corresponding to 300 different outputs in 75 time steps from $z = 4.19$ –3.00). We compared the simulated LIS line properties and profiles to the observed spectra of the 45 low-redshift star-forming galaxies from CLASSY (Berg et al. 2022) to investigate if and how such a simulation setup can be used as a laboratory to interpret spectroscopic observations. We summarize our findings as follows:

1. The range of the C II and Si II resonant line properties (equivalent width, residual flux, and central velocity) seen in the simulated spectra overlaps with 39 out of 45 CLASSY galaxies (Section 3, Figure 4). The six remaining objects have either too large EW(C II) and EW(Si II), or too large $v_{\text{cen}}(\text{C II})$ and $v_{\text{cen}}(\text{Si II})$ compared to the simulated spectra. Five of them have stellar masses larger than the $\sim 10^9 M_\odot$ simulated galaxy.
2. We identified a mock spectrum that closely matches the observed absorption and emission line profile for 28 CLASSY galaxies. For nine galaxies, the best-matched mock spectrum matches well the absorption feature but overpredicts the fluorescent emission. For seven galaxies (including the six objects with either too large EWs or v_{cen}), the best-matched mock spectrum poorly reproduces both the absorption and fluorescent features. In general, the mock spectra do not match well the LIS line spectra
3. We show that accounting for the COS aperture size faithfully solves the tension between the amount of fluorescent emission in the simulation and in the CLASSY observations. This is because fluorescent emission is more extended than the UV continuum (Section 4.1) and a small aperture centered on the UV peak will miss a significant fraction of scattered light. Using mock spectra extracted using a fiducial aperture whose size corresponds to the actual size of the COS aperture, we show significant improvements in reproducing the fluorescent emission in eight CLASSY observations (Section 4.2).
4. The typical LIS line shape and properties seen in the simulated galaxy vary significantly both with time and per viewing angle (Section 5.1). In particular, we highlighted the connection between the fluctuations of the Si II properties and the evolution of the galaxy SFR, which suggests that the combination of several physical processes (e.g., star formation bursts, feedback mechanisms, gas accretion) may lead to large spatial and temporal variability in the ISM properties. This explains how the evolution of a single galaxy at $z \sim 3$ can produce such a diversity of line profiles that replicate the spectra of 38 out of the 45 low-redshift CLASSY galaxies spanning a broad range of galaxy properties (M_\star between 10^6 and $10^9 M_\odot$ and Z_{gas} between 0.02 and 0.55 Z_\odot).
5. We explored the spatial origin of the continuum, residual flux, and fluorescent emission in the mock spectra that best match the spectra of J0926+4427 and J0938+5428 (Section 5.2). We showed that there is little overlap in the

of the CLASSY galaxies with a stellar mass larger than the simulated galaxy, suggesting that the latter does not represent well more massive galaxies (Section 3.2).

3. We show that accounting for the COS aperture size faithfully solves the tension between the amount of fluorescent emission in the simulation and in the CLASSY observations. This is because fluorescent emission is more extended than the UV continuum (Section 4.1) and a small aperture centered on the UV peak will miss a significant fraction of scattered light. Using mock spectra extracted using a fiducial aperture whose size corresponds to the actual size of the COS aperture, we show significant improvements in reproducing the fluorescent emission in eight CLASSY observations (Section 4.2).
4. The typical LIS line shape and properties seen in the simulated galaxy vary significantly both with time and per viewing angle (Section 5.1). In particular, we highlighted the connection between the fluctuations of the Si II properties and the evolution of the galaxy SFR, which suggests that the combination of several physical processes (e.g., star formation bursts, feedback mechanisms, gas accretion) may lead to large spatial and temporal variability in the ISM properties. This explains how the evolution of a single galaxy at $z \sim 3$ can produce such a diversity of line profiles that replicate the spectra of 38 out of the 45 low-redshift CLASSY galaxies spanning a broad range of galaxy properties (M_\star between 10^6 and $10^9 M_\odot$ and Z_{gas} between 0.02 and 0.55 Z_\odot).
5. We explored the spatial origin of the continuum, residual flux, and fluorescent emission in the mock spectra that best match the spectra of J0926+4427 and J0938+5428 (Section 5.2). We showed that there is little overlap in the

regions contributing to each spectral feature, and the properties of these regions also vary depending on the galaxy orientation. This analysis demonstrates that integrated LIS line spectra are complex combinations of multiple, spatially distinct components, which makes their interpretation difficult. Yet, the present simulation presents an optimal framework for understanding and analyzing spectroscopic observations.

Overall, this work challenges simplified interpretations of down-the-barrel spectra but introduces a new methodology where high-resolution simulations can help us understand physically motivated scenarios that explain the observations. In particular, the remarkable success of reproducing real observations with mock spectra from RHD-RT simulations opens diverse and extremely promising perspectives for follow-up analyses. In future work, we will first explore how using different radiative-transfer recipes (e.g., diverse dust opacity and turbulent velocity models) impact our results in order to determine the crucial physical ingredients needed to reproduce observations of star-forming galaxies. Second, we will extend the analysis of the physical and spatial origin of the different spectral features in the simulation. This effort will enable us to tighten our understanding of how absorption and emission line diagnostics relate to gas kinematics (in particular, the importance of outflows) and to the escape of ionizing photons. This work will look simultaneously at the LIS line and Ly α profiles, building upon the work of Blaizot et al. (2023). Finally, we plan to use spatially resolved observations with KCWI and MUSE to further assess the simulation’s predictions on the spatial origin of the different spectral features that compose the LIS metal line spectra.

Acknowledgments

The authors would like to thank the referee for thoughtful feedback that improved the quality of this manuscript. S.G. is grateful for the support enabled by the Harlan J. Smith McDonald fellowship, which made this project possible. T.G. and A.V. are supported by the professorship grant SNFProf_PP00P2_211023 from the Swiss National Foundation for Scientific Research. V.M. acknowledges support from the NWO grant 016.VIDI.189.162

(“ODIN”). Observations for this paper come from HST-GO-15840. C.L.M. acknowledges support from NSF under AST-1817125. B.L.J. is thankful for support from the European Space Agency (ESA). We are grateful for the support of this program that was provided by NASA through a grant from the Space Telescope Science Institute, which is operated by the Associations of Universities for Research in Astronomy, Incorporated, under NASA contract NASS-26555.

Facility: HST(COS).

Software: Astropy (Astropy Collaboration et al. 2022), NumPy (Harris et al. 2020), pandas (McKinney 2010), SciPy (Virtanen et al. 2020), Photutils (Bradley et al. 2020), RASCAS (Michel-Dansac et al. 2020).

Appendix A

Further Discussion of the Trends Observed in Figure 3

In Section 3, we discussed the origin of several trends between the C II and Si II properties shown in Figure 4. In particular, we noted that EW(C II) is typically smaller than EW(Si II) in spectra with weak absorption lines (EWs < 1 Å). A similar behavior is observed for $v_{\text{cen}}(\text{C II})$ versus $v_{\text{cen}}(\text{Si II})$. Additionally, we found that $R_f(\text{C II})$ is often found larger than $R_f(\text{Si II})$. As we noted in Section 3, all these trends can be explained by the impact of the C II* $\lambda 1335$ features on the EW(C II $\lambda 1334$) measurements. Spectra with significant C II* fluorescent emission will have lower EW(C II), $v_{\text{cen}}(\text{C II})$, and $R_f(\text{C II})$ because the emission fills a significant portion of the absorption line. C II $\lambda 1334$ lines are affected by infilling due to resonant scattering, typically more than for the Si II $\lambda 1260$ lines, the combination of both effects yielding C II absorption lines considerably weaker in that regime. On the other way, spectra with broad C II $\lambda 1334$ absorption lines commonly have a significant absorption around the fluorescent wavelength. The combined resonant and fluorescent absorption feature yields large EW(C II) and redder $v_{\text{cen}}(\text{C II})$, sometimes mimicking the presence of significant inflowing gas. This scenario less significantly impacts R_f because the minimum C II $\lambda 1334$ flux is often deeper for the fluorescent absorption line. Figure 13 provides two examples of these configurations using mock spectra generated in this work.

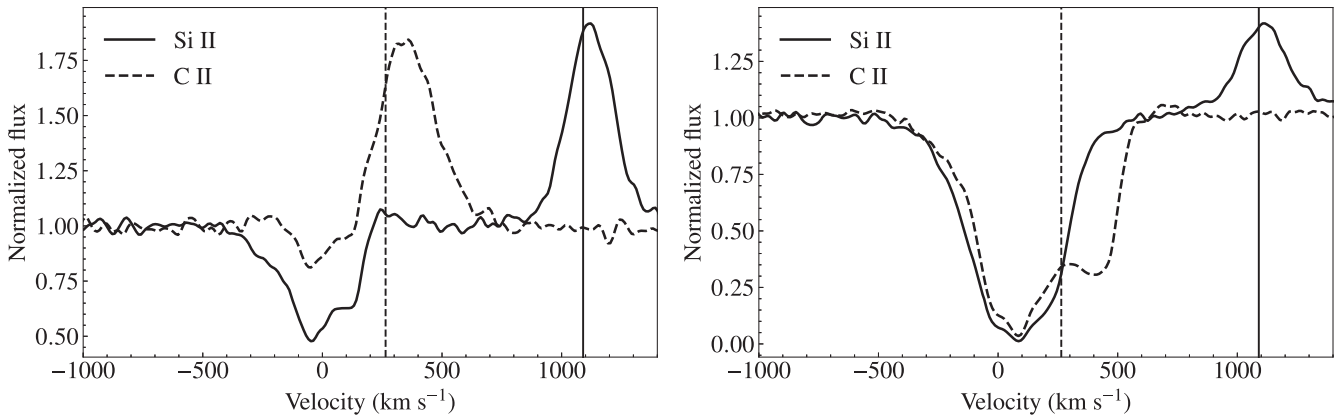


Figure 13. Comparisons of mock C II and Si II spectra (dotted and solid lines, respectively, with vertical lines showing the expected wavelength of the fluorescent feature for each ion) for two configurations. In the left panel, both spectra exhibit a considerable fluorescent emission feature. For C II, because of the small wavelength separation between the resonance and fluorescent channel, this emission fills a large portion of the absorption line. As we note in the text, resonant scattering infilling, which is stronger for C II than for Si II, also plays a role in producing weaker C II $\lambda 1334$ lines. Overall, the analysis of the combined spectrum will yield $|\text{EW}(\text{C II } \lambda 1334)| < |\text{EW}(\text{Si II } \lambda 1260)|$ and $R_f(\text{C II } \lambda 1334) < R_f(\text{Si II } \lambda 1260)$. The right panel shows a different case where the C II* $\lambda 1335$ feature is in absorption. While we observe $R_f(\text{C II } \lambda 1334) \approx R_f(\text{Si II } \lambda 1260)$, suggesting the fluorescent absorption has little impact on $R_f(\text{C II } \lambda 1334)$, this scenario will yield $|\text{EW}(\text{C II } \lambda 1334)| > |\text{EW}(\text{Si II } \lambda 1260)|$ and $v_{\text{cen}}(\text{C II } \lambda 1334) > v_{\text{cen}}(\text{Si II } \lambda 1260)$. These different configurations are responsible for the mock spectra trends seen in Figure 4.

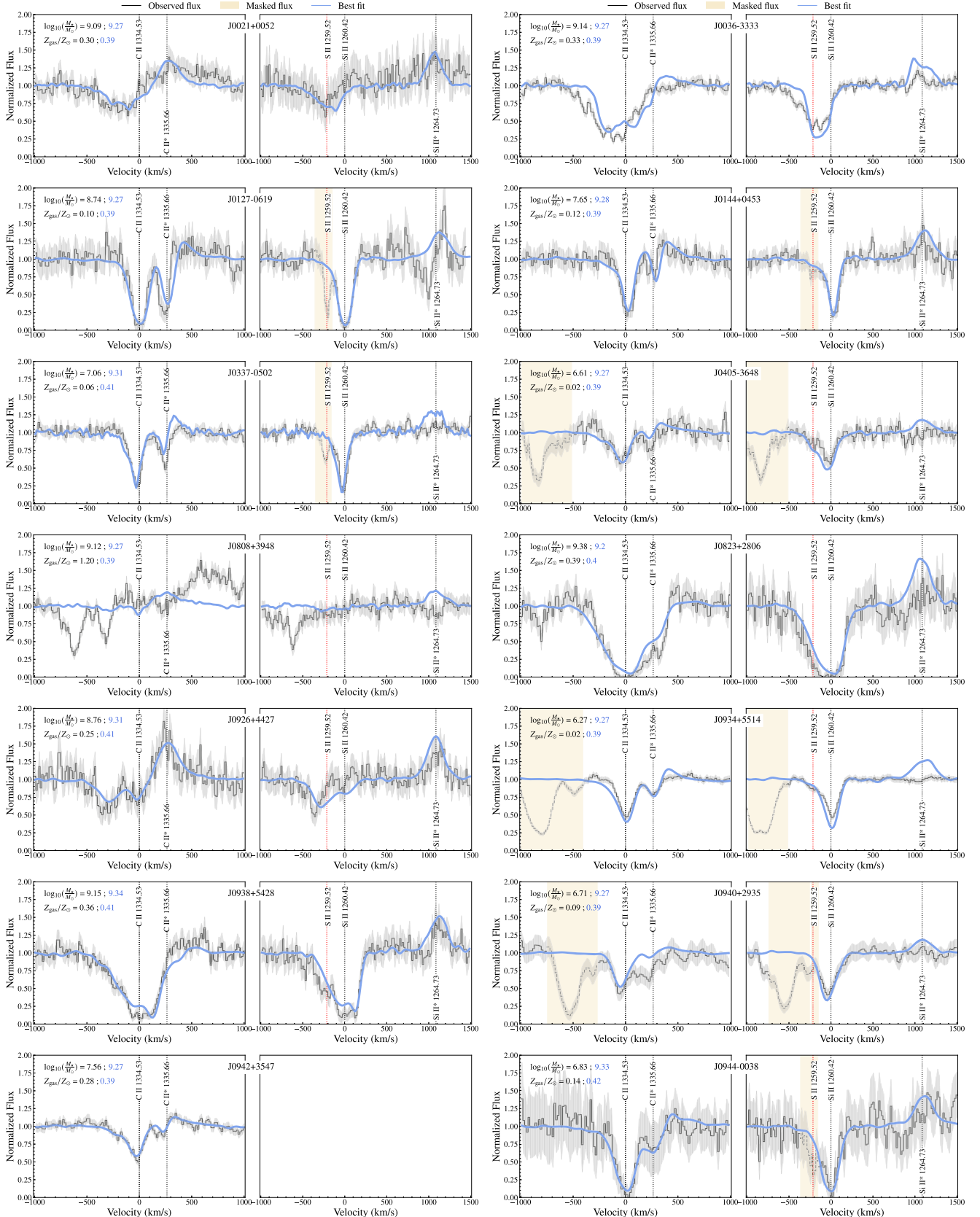


Figure 14. The fits of the $\text{C II} \lambda 1334 + \text{C II}^* \lambda 1335$ (left panels) and $\text{Si II} \lambda 1260 + \text{Si II}^* \lambda 1265$ (right panels) line profiles for all CLASSY galaxies using the procedure detailed in Section 3.2. The black line denotes the observed flux, the gray dashed line shows regions that are masked, and the gray shaded area denotes the flux error. The vertical dotted lines indicate the expected location of each transition. The blue line represents the best mock spectrum found, i.e., the mock spectrum with the lower χ^2 based on Equation (2). In the top left corner of the left panels, we detail the stellar mass and gas metallicity of the classy galaxy (in black) and of the virtual galaxy at the time step where the best fit has been found (in blue).

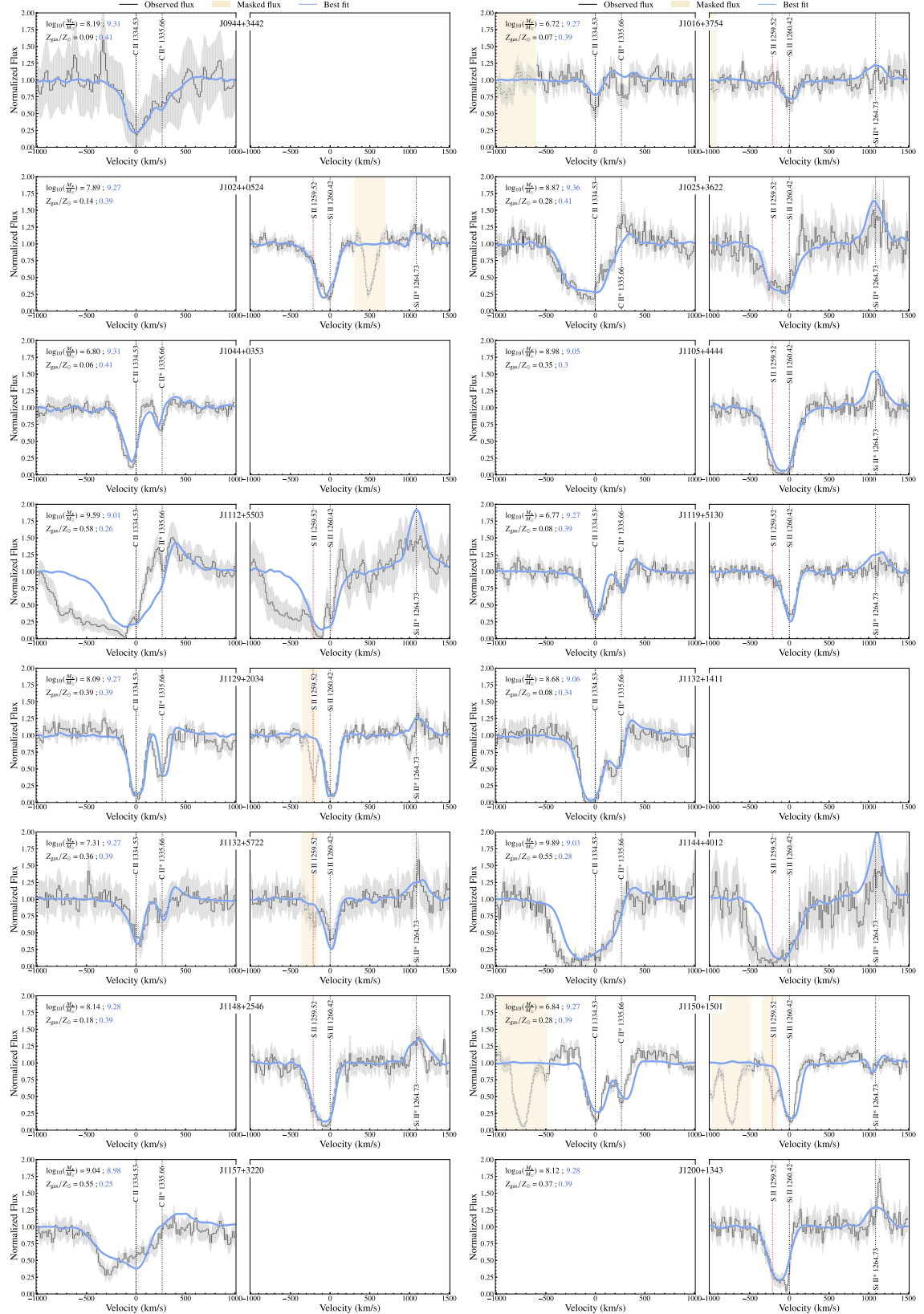


Figure 14. (Continued.)

The blending of the C II $\lambda 1334$ and C II* $\lambda 1335$ contributions can explain the C II and Si II trends observed in the simulation, yet, we also find that the CLASSY measurements do seem to follow

slightly different trends. In particular, we find that the classy objects typically have $EW(Si\,II) > EW(C\,II)$, $v_{cen}(Si\,II) > v_{cen}(C\,II)$, and $R(C\,II) \approx R(Si\,II)$. The two former trends can be explained by the

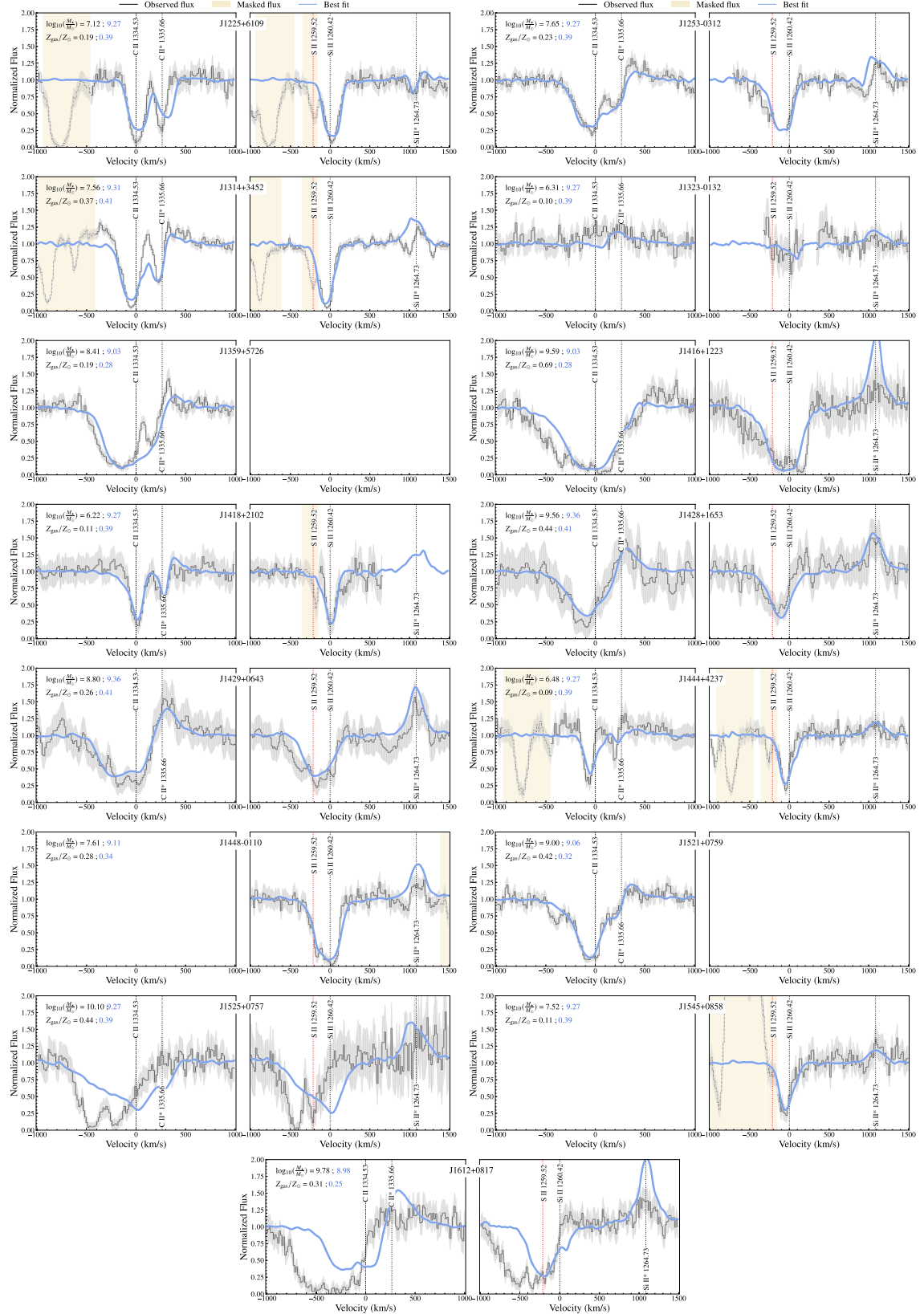


Figure 14. (Continued.)

presence of the S II absorption line blended with the Si II $\lambda 1260$ line, which contribution is not modeled in the simulated spectra. This additional absorption on the blue side biases the EW(Si II) and

$v_{\text{cen}}(\text{Si II})$ toward larger and lower values, respectively. The spectra of J1129+2904, shown in Figure 14, nicely illustrate the impact of S II absorption line on the Si II $\lambda 1260$ line.

Appendix B Best-fit Mock Spectra

B.1. Using the Matching Approach of Section 3.2

Figure 14 presents the spectra that best match the CLASSY Si II and C II observations using the approach detailed in Section 3.2. As discussed in the latter section, the best fits reproduce accurately the absorption features seen in the observations but overestimate the contribution of the fluorescent emission for 6 of 39 galaxies.

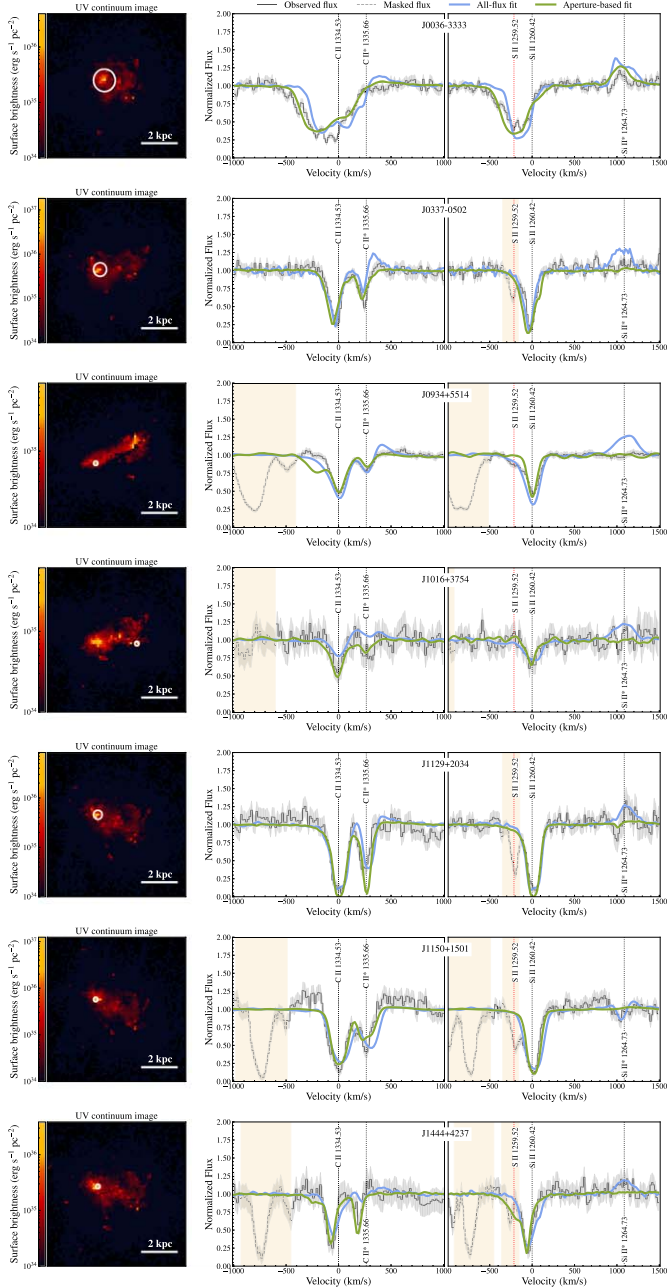
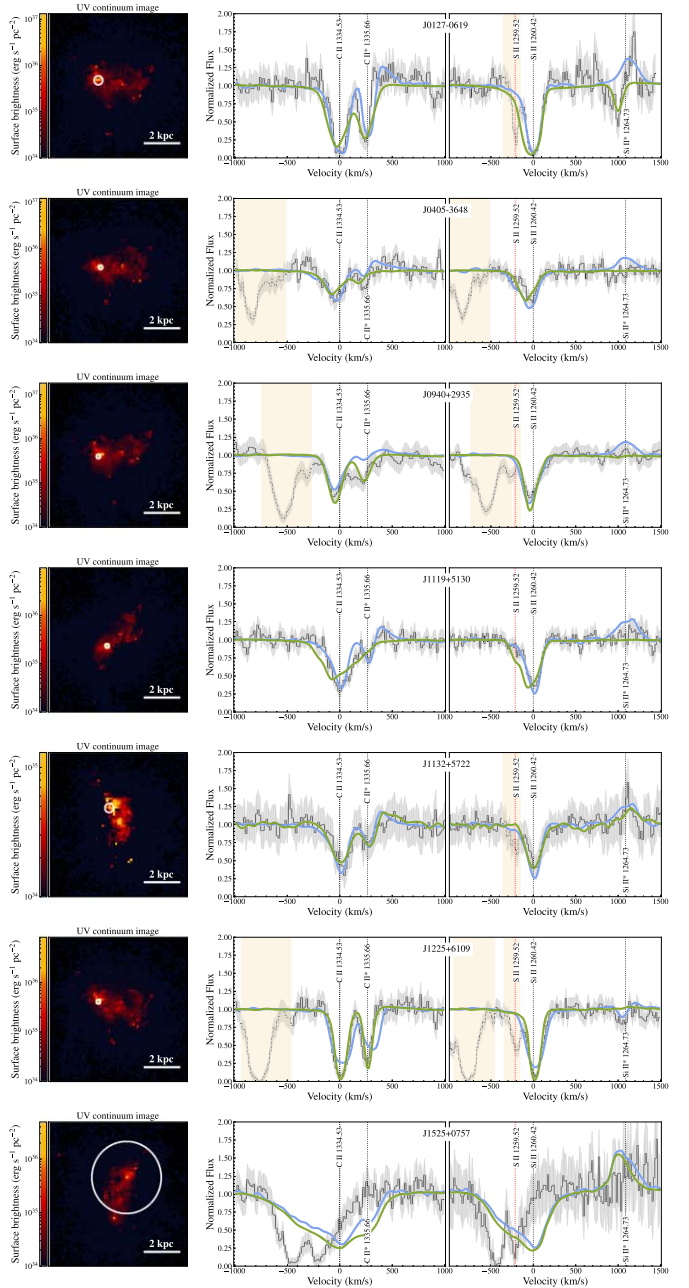


Figure 15. Comparison of the C II $\lambda 1334 + \text{C II}^* \lambda 1335$ (middle panels) and Si II $\lambda 1260 + \text{Si II}^* \lambda 1265$ (right panels) fits for the 16 CLASSY galaxies which have $r_{50}/1.25 > 1$ and observations for both Si II and C II. The blue line (all-flux fit) is the best-fit mock spectrum found in Section 3.2, the green line (aperture-based fit) is the best-fit mock spectrum obtained using a fiducial aperture size corresponding to the COS aperture size at the galaxy redshift. The location and size of the region from which the green spectrum is extracted are shown with a black circle on the left panel.

B.2. Using the Fitting Approach of Section 4.2

Figure 15 presents the best fits of the CLASSY Si II and C II spectra using the approach detailed in Section 4.2. The fitting approach is done using a single simulation output where the mock spectra are extracted using circular apertures of which size corresponds to the size of the COS aperture at the galaxy redshift. As discussed in Section 4.2, this refined approach enables improvement of the fits around the fluorescent wavelengths. We note that for this experiment, we only considered galaxies that have observations for both Si II and



C II, and have $r_{50}/1.25$ values larger than 1 (i.e., potentially significantly impacted by aperture loss, see Section 4.1).

Appendix C Comparison of the UV and Optical Half-light Radii

In this section, we estimate and compare the half-light radii estimated from the UV continuum and from the optical continuum for the virtual galaxy. Using the simulation output at $t = 2$ Gyr, we extract the SB profiles at 1270 and at 3500 Å for the UV and optical, for each of the 300 lines of sight available. Figure 16 shows the median and standard deviation of the 300 UV and optical SB profiles. For each of the 300 SB profiles, we derive the corresponding r_{50}^{UV} and r_{50}^{opt} and derive the median and standard deviation of the 300 values. We find that $r_{50}^{\text{UV}} \approx r_{50}^{\text{opt}}$.

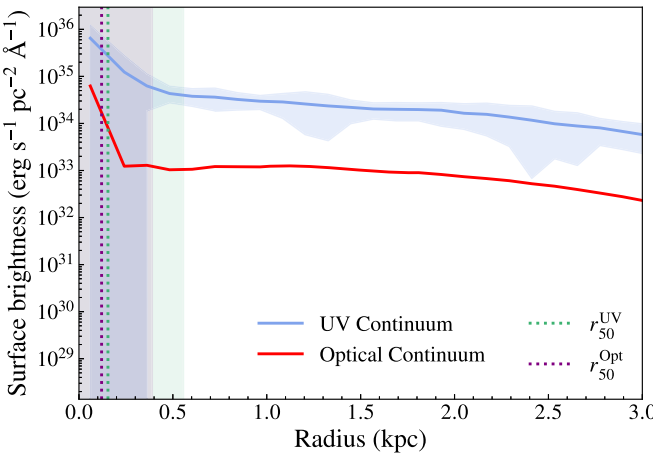


Figure 16. The light curves of the UV and optical continuum derived using the average and standard deviation of 300 line-of-sight images of the galaxy at 1270 and 3500 Å, respectively. Despite differences regarding the total brightness seen at both wavelengths, the median UV and optical half-light radii determined from these curves only differ by a few parsecs.

ORCID iDs

Simon Gazagnes [DOI](https://orcid.org/0000-0002-5659-4974)

Valentin Mauerhofer [DOI](https://orcid.org/0000-0003-0595-9483)

Danielle A. Berg [DOI](https://orcid.org/0000-0002-4153-053X)

Jeremy Blaizot [DOI](https://orcid.org/0000-0003-1609-7911)

Anne Verhamme [DOI](https://orcid.org/0000-0002-2201-1865)

Thibault Garel [DOI](https://orcid.org/0000-0002-9613-9044)

Dawn K. Erb [DOI](https://orcid.org/0000-0001-9714-2758)

Karla Z. Arellano-Córdova [DOI](https://orcid.org/0000-0002-2644-3518)

Jarle Brinchmann [DOI](https://orcid.org/0000-0003-4359-8797)

John Chisholm [DOI](https://orcid.org/0000-0002-0302-2577)

Matthew Hayes [DOI](https://orcid.org/0000-0001-8587-218X)

Alaina Henry [DOI](https://orcid.org/0000-0002-6586-4446)

Bethan L. James [DOI](https://orcid.org/0000-0003-4372-2006)

Anne Jaskot [DOI](https://orcid.org/0000-0002-6790-5125)

Nika Jurlin [DOI](https://orcid.org/0000-0003-4270-5968)

Crystal L. Martin [DOI](https://orcid.org/0000-0001-9189-7818)

Michael Maseda [DOI](https://orcid.org/0000-0003-0695-4414)

Claudia Scarlata [DOI](https://orcid.org/0000-0002-9136-8876)

Evan D. Skillman [DOI](https://orcid.org/0000-0003-0605-8732)

Stephen M. Wilkins [DOI](https://orcid.org/0000-0003-3903-6935)

Aida Wofford [DOI](https://orcid.org/0000-0001-8289-3428)

Xinfeng Xu [DOI](https://orcid.org/0000-0002-9217-7051)

References

- Alexandroff, R. M., Heckman, T. M., Borthakur, S., Overzier, R., & Leitherer, C. 2015, *ApJ*, **810**, 104
- Arellano-Córdova, K. Z., Mingozi, M., Berg, D. A., et al. 2022, *ApJ*, **935**, 74
- Asplund, M., Amarsi, A. M., & Grevesse, N. 2021, *A&A*, **653**, A141
- Astropy Collaboration, Price-Whelan, A. M., Lim, P. L., et al. 2022, *ApJ*, **935**, 167
- Badnell, N. R. 2006, *ApJS*, **167**, 334
- Berg, D. A., James, B. L., King, T., et al. 2022, *ApJS*, **261**, 31
- Blaizot, J., Garel, T., Verhamme, A., et al. 2023, *MNRAS*, **523**, 3749
- Bosman, S. E. I., Laporte, N., Ellis, R. S., Ouchi, M., & Harikane, Y. 2019, *MNRAS*, **487**, L67
- Bradley, L., Sipőcz, B., Robitaille, T., et al. 2020, astropy/photutils: 1.0.0, v1.0.0, Zenodo, doi:[10.5281/zenodo.4044744](https://doi.org/10.5281/zenodo.4044744)
- Carr, C., & Scarlata, C. 2022, *ApJ*, **939**, 47
- Carr, C., Scarlata, C., Panagia, N., & Henry, A. 2018, *ApJ*, **860**, 143
- Chisholm, J., Gazagnes, S., Schaerer, D., et al. 2018, *A&A*, **616**, A30
- Chisholm, J., Orlitová, I., Schaerer, D., et al. 2017a, *A&A*, **605**, A67
- Chisholm, J., Tremonti, C. A., Leitherer, C., & Chen, Y. 2017b, *MNRAS*, **469**, 4831
- Chisholm, J., Tremonti, C. A., Leitherer, C., Chen, Y., & Wofford, A. 2016, *MNRAS*, **457**, 3133
- Chisholm, J., Tremonti, C. A., Leitherer, C., et al. 2015, *ApJ*, **811**, 149
- Choban, C. R., Kereš, D., Hopkins, P. F., et al. 2022, *MNRAS*, **514**, 4506
- De Cia, A., Ledoux, C., Mattsson, L., et al. 2016, *A&A*, **596**, A97
- Du, X., Shapley, A. E., Topping, M. W., et al. 2021, *ApJ*, **920**, 95
- Eldridge, J. J., Izzard, R. G., & Tout, C. A. 2008, *MNRAS*, **384**, 1109
- Erb, D. K., Pettini, M., Shapley, A. E., et al. 2010, *ApJ*, **719**, 1168
- Erb, D. K., Quider, A. M., Henry, A. L., & Martin, C. L. 2012, *ApJ*, **759**, 26
- Faucher-Giguère, C.-A., Lidz, A., Zaldarriaga, M., & Hernquist, L. 2009, *ApJ*, **703**, 1416
- Finley, H., Bouché, N., Contini, T., et al. 2017a, *A&A*, **605**, A118
- Finley, H., Bouché, N., Contini, T., et al. 2017b, *A&A*, **608**, A7
- Gatkine, P., Veilleux, S., & Cucchiara, A. 2019, *ApJ*, **884**, 66
- Gazagnes, S., Chisholm, J., Schaerer, D., et al. 2018, *A&A*, **616**, A29
- Grassi, T., Bovino, S., Schleicher, D. R. G., et al. 2014, *MNRAS*, **439**, 2386
- Grevesse, N., Asplund, M., Sauval, A. J., & Scott, P. 2010, *Ap&SS*, **328**, 179
- Hahn, O., & Abel, T. 2013, MUSIC: Multi-Scale Initial Conditions, Astrophysics Source Code Library, ascl:[1311.011](https://ascl.net/1311.011)
- Harris, C. R., Millman, K. J., van der Walt, S. J., et al. 2020, *Natur*, **585**, 357
- Heckman, T. M., Alexandroff, R. M., Borthakur, S., Overzier, R., & Leitherer, C. 2015, *ApJ*, **809**, 147
- Heckman, T. M., Lehnert, M. D., Strickland, D. K., & Armus, L. 2000, *ApJS*, **129**, 493
- Heckman, T. M., Sembach, K. R., Meurer, G. R., et al. 2001, *ApJ*, **558**, 56
- James, B., & Aloisi, A. 2018, *ApJ*, **853**, 124
- James, B. L., Aloisi, A., Heckman, T., Sohn, S. T., & Wolfe, M. A. 2014, *ApJ*, **795**, 109
- James, B. L., Berg, D. A., King, T., et al. 2022, *ApJS*, **262**, 37
- Jaskot, A. E., Dowd, T., Oey, M. S., Scarlata, C., & McKinney, J. 2019, *ApJ*, **885**, 96
- Jaskot, A. E., & Oey, M. S. 2014, *ApJL*, **791**, L19
- Jenkins, E. B. 2009, *ApJ*, **700**, 1299
- Jones, T., Stark, D. P., & Ellis, R. S. 2012, *ApJ*, **751**, 51
- Katz, H., Liu, S., Kimm, T., et al. 2022, arXiv:[2211.04626](https://arxiv.org/abs/2211.04626)
- Konstantopoulou, C., De Cia, A., Krogager, J.-K., et al. 2022, *A&A*, **666**, A12
- Lebouteiller, V., Heap, S., Hubeny, I., & Kunth, D. 2013, *A&A*, **553**, A16
- Luridiana, V., Morisset, C., & Shaw, R. A. 2015, *A&A*, **573**, A42
- Martin, C. L., Shapley, A. E., Coil, A. L., et al. 2012, *ApJ*, **760**, 127
- Mauerhofer, V. 2021, PhD thesis, Univ. Geneva, <https://theses.hal.science/tel-03901797>
- Mauerhofer, V., Verhamme, A., Blaizot, J., et al. 2021, *A&A*, **646**, A80
- McKinney, W. 2010, in Proc. 9th Python in Science Conf. Data Structures for Statistical Computing in Python, ed. S. van der Walt & J. Millman, 56
- Michel-Dansac, L., Blaizot, J., Garel, T., et al. 2020, *A&A*, **635**, A154
- Oppenheimer, B. D., Davé, R., Kereš, D., et al. 2010, *MNRAS*, **406**, 2325
- Parvathi, V. S., Sofia, U. J., Murthy, J., & Babu, B. R. S. 2012, *ApJ*, **760**, 36
- Prochaska, J. X., Kasen, D., & Rubin, K. 2011, *ApJ*, **734**, 24
- Reddy, N. A., Steidel, C. C., Pettini, M., Bogosavljević, M., & Shapley, A. E. 2016, *ApJ*, **828**, 108
- Rémy-Ruyer, A., Madden, S. C., Galliano, F., et al. 2014, *A&A*, **563**, A31
- Rivera-Thorsen, T. E., Dahle, H., Gronke, M., et al. 2017, *A&A*, **608**, L4

- Rivera-Thorsen, T. E., Hayes, M., Östlin, G., et al. 2015, *ApJ*, **805**, 14
- Rosdahl, J., Blaizot, J., Aubert, D., Stranex, T., & Teyssier, R. 2013, *MNRAS*, **436**, 2188
- Rosdahl, J., Katz, H., Blaizot, J., et al. 2018, *MNRAS*, **479**, 994
- Rosdahl, J., & Teyssier, R. 2015, *MNRAS*, **449**, 4380
- Rubin, K. H. R., Prochaska, J. X., Ménard, B., et al. 2011, *ApJ*, **728**, 55
- Saldana-Lopez, A., Schaefer, D., Chisholm, J., et al. 2022, *A&A*, **663**, A59
- Scarlata, C., & Panagia, N. 2015, *ApJ*, **801**, 43
- Schwartz, C. M., Martin, C. L., Chandar, R., et al. 2006, *ApJ*, **646**, 858
- Shapley, A. E., Steidel, C. C., Pettini, M., & Adelberger, K. L. 2003, *ApJ*, **588**, 65
- Stanway, E. R., Eldridge, J. J., & Becker, G. D. 2016, *MNRAS*, **456**, 485
- Steidel, C. C., Bogosavljević, M., Shapley, A. E., et al. 2018, *ApJ*, **869**, 123
- Teyssier, R. 2002, *A&A*, **385**, 337
- Trebitsch, M., Blaizot, J., Rosdahl, J., Devriendt, J., & Slyz, A. 2017, *MNRAS*, **470**, 224
- Trebitsch, M., Dubois, Y., Volonteri, M., et al. 2021, *A&A*, **653**, A154
- Vasei, K., Siana, B., Shapley, A. E., et al. 2016, *ApJ*, **831**, 38
- Verner, D. A., Ferland, G. J., Korista, K. T., & Yakovlev, D. G. 1996, *ApJ*, **465**, 487
- Virtanen, P., Gommers, R., Oliphant, T. E., et al. 2020, *NatMe*, **17**, 261
- Voronov, G. S. 1997, *ADNDT*, **65**, 1
- Wang, B., Heckman, T. M., Zhu, G., & Norman, C. A. 2020, *ApJ*, **894**, 149
- Wofford, A., Leitherer, C., & Salzer, J. 2013, *ApJ*, **765**, 118
- Wolfe, A. M., Prochaska, J. X., & Gawiser, E. 2003, *ApJ*, **593**, 215
- Xu, X., Heckman, T., Henry, A., et al. 2022, *ApJ*, **933**, 222
- Xu, X., Heckman, T., Henry, A., et al. 2023, *ApJ*, **948**, 28